Commissioning of ThomX Compton source subsystems and demonstration of 10^{10} x-rays/s

Muath Alkadi, Manuel Alves, Manar Amer, Loic Amoudry, Didier Auguste, Jean-Luc Babigeon, Michel Baltazar, Alain Benoit, Alexandre Blin, Marco Bonanzingamarco, Jean Bonenfant, Julien Bonis, Jean-Pierre Brasile, Kevin Cassou, Jean-Noël Cayla, Thomas Chabaud, Iryna Chaikovska, Sophie Chance, Vincent Chaumat, Ronic Chiche, Patrick Cornebise, Olivier Dalifard, Nicolas Delerue, Remy Dorkel, Denis Douillet, Illya Drebot, Jean-Phillipe Dugal, Kevin Dupraz, Noureddine El Kamchi, Mohamed El Khaldi, Ezgi Ergenlik, Pierre Favier, Marco Fernandez, Alexis Gamelin, Jean-Francois Garaut, Luca Garolfi, Philippe Gauron, Frédéric Gauthier, Alexandre Gonnin, Denis Grasset, Eric Guerard, Hayg Guler, Jacques Haissinski, Emmanuel Herry, Gregory Iaquaniello, Marie Jacquet,* Didier Jehanno, Eric Jules, Viacheslav Kubytskyi, François Labaye, Mickaël Lacroix, Marc Langlet, Titouan Lebarillec, Jean-François Ledu, Damien Le Guidec, Bruno Leluan, Pierre Lepercq, Frédéric Letellier-cohen, Rodolphe Marie, Jean-Claude Marrucho, Aurélien Martens, Christophe Mageur, Gabriel Mercadier, Bruno Mercier, Eric Mistretta, Hugues Monard, Alexandre Moutardier, Viktor Mytrochenko, Olivier Neveu, Daniele Nutarelli, Maher Omeich, Yann Peinaud, Antoine Pérus, Yannick Petrilli, Marc Pichet, Bernard Pieyre, Eric Plaige, Christophe Prévost, Thomas Roulet, Raphael Roux, Philippe Rudnicky, Viktor Soskov, Monique Taurigna-Quéré, Stéphane Trochet, Cynthia Vallerand, Alessandro Variola, Olivier Vitez, François Wicek, Guy Wormser, Sébastien Wurth, and Fabian Zomer

IJCLab, Université Paris-Saclay/CNRS/IN2P3, Orsay, France

Patrick Alexandre, Rachid Ben el Fekih, Philippe Berteaud, Sébastien Bobault, Yazid Bouanani, François Bouvet, Lodovico Cassinari, Marie-Emmanuelle Couprie, Renaud Cuoq, Helder Dias, Yannick Dietrich, Massamba Diop, Eric Dupuy, Moussa El Ajjouri, Christian Herbeaux, Nicolas Hubert, Marie Labat, Alain Lestrade, Antoine Letrésor, Robert Lopes, Alexandre Loulergue, Patrick Marchand, Fabrice Marteau, Didier Muller, Amor Nadji, Laurent Nadolski, Ryutaro Nagaoka, Dominique Pedeau, Sylvain Petit, Jean Pierre Pollina, Fernand Ribeiro, Manuel Ros, Julien Salvia, Mourad Sebdaoui, Rajesh Sreedharan, Jean Susini, and José Veteran

SOLEIL Synchrotron, Saint-Aubin, France

Cyril Bruyere, Alain Cobessi, William Del Net, Jean-Louis Hazemann, Jean-Louis Hodeau, Philippe Jacquet, Philippe Jeantet, Grigor Kapoujyan, Jérôme Lacipière, Eric Lahéra, Gilles Perroux, Olivier Proux, and Emmanuel Roy

Institut Néel, Université Grenoble Alpes/CNRS, Grenoble, France

Philippe Walter

LAMS, Sorbonne Université/CNRS, Paris, France

Alberto Bravin

University of Milano-Bicocca, Milano, Italy and University of Calabria, Rende, Italy

Hélène Elleaume and François Estève

STROBE, Université Grenoble Alpes/INSERM, Grenoble, France

Harold Bzyl, Christophe Chapelle, Jean-Michel Horodynski, and Pierre Robert

IRSD, Université Paris-Saclay/CNRS, Orsay, France

Eric Cormier

LP2N, Université de Bordeaux/CNRS, Bordeaux, France

Jérôme Degallaix, Christophe Michel, and Laurent Pinard
LMA, Université de Lyon/CNRS, Villeurbanne, France

Philippe Balcou, Jérôme Lhermite, Sébastien Montant, Marie-Christine Nadeau, and Stéphane Petit
CELIA, Université de Bordeaux/CNRS/CEA, Talence, France

Nikolay Artemiev
LOA, ENSTA/Ecole Polytechnique/CNRS, Palaiseau, France

Marica Biagini
INFN, Rome, Italy

Romain Czarny, Pascal Girault, Sophie Muller, Serge Sierra, and Christophe Simon-Boisson
THALES, Vélizy, France

Said Bouaziz
IRFU, Université Paris-Saclay/CEA, Gif-sur-Yvette, France

Chamseddine Benabderrahmane and Géraldine Le Duc
ESRF Synchrotron, Grenoble, France

Xing Liu
DEP, Tsinghua University, Beijing, China

(Received 6 September 2024; accepted 17 December 2024; published 7 February 2025)

ThomX is a compact x-ray source based on Compton scattering, installed at IJCLab (Laboratoire de physique des 2 infinis-Irène Joliot-Curie) in Orsay. The machine uses a small electron storage ring and an intense laser pulse stored in a high-finesse optical cavity. This article describes the various subsystems of the machine and their initial results of the commissioning, which began in mid-2021. This first commissioning phase led to the production of 10^{10} x-rays/s with an on-axis energy of 45 keV. The main steps to be taken to reach the nominal flux are outlined at the end.

DOI: 10.1103/PhysRevAccelBeams.28.023401

I. INTRODUCTION

Compact Compton sources are machines of modest size ($\sim$100 m^2) capable of delivering a high-flux ($> 10^{10}$ ph/s), quasimonochromatic (few % of bandwidth) x-ray beam with brightness several orders of magnitude greater than the conventional laboratory sources. Even if Compton source fluxes cannot compete with synchrotron radiation sources, the cost and compactness of these machines make them attractive for a wide spectrum of applications in the fields of medicine (imaging and therapy), biology, cultural heritage (studies and preservation), or industry [1,2]. Compton x-rays are generated by the interaction of an electron bunch and a laser pulse. With the development of this type of source, many experiments currently only carried out at synchrotron facilities could be performed in a laboratory, museum, or hospital [3]. The ThomX project, carried by IJCLab, is the French demonstrator of such a source. It is installed on the Paris-Saclay university campus. To produce a high x-ray flux with ThomX, electron bunches and laser pulses are stored in a storage ring and a high-gain Fabry-Perot cavity, respectively [4,5]. Pioneering work at IJCLab and the laboratory's experience in the field of interactions between ultrarelativistic electrons and a high-power laser beam in an optical cavity (< several tens of kW) dates back many years [6–9].

The layout of the ThomX machine is presented in Fig. 1. For radiation protection purposes, the machine is installed inside a shielded zone, the bunker, made up of thick concrete walls. An electron bunch of up to 1 nC charge (nominal value) with an energy of $\sim$5 MeV emitted by a photoinjector at a repetition frequency of 50 Hz is accelerated to an energy range from 50 to 70 MeV, then passed

*Contact author: marie.jacquet@ijclab.in2p3.fr

Published by the American Physical Society under the terms of the Creative Commons Attribution 4.0 International license. Further distribution of this work must maintain attribution to the author(s) and the published article's title, journal citation, and DOI.

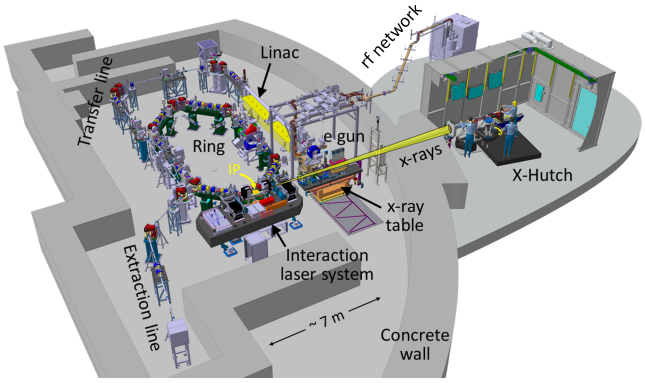

FIG. 1. Layout of the ThomX source.

in a transfer line to be injected and stored in a small ring, 18 m in circumference, during 20 ms. The storage ring operates nominally at 50 Hz to completely replace the recirculating electron bunch, the injection is performed with a single bunch, and no radiation damping exists. After 20 ms the circulating bunch is ejected from the ring in an extraction line toward the final dump, and a new bunch is injected. The nominal normalized emittance of the electron bunch at the interaction point (IP) is 6–7 π mm mrad and 25–30 π mm mrad at the beginning and the end of the storage time, respectively. At the IP, the bunch interacts each turn with a laser pulse. The laser system consists of a laser oscillator designed for delivering pulses amplified to around 70 W and accumulated in the optical cavity to reach up to 700 kW. The two beams cross every 60 ns with an angle of incidence equal to 2°. A system of synchronization coordinates all subsystems of the machine.

The x-ray flux, N_X, generated by Compton scattering is written as follows:

$$N_X \sim \sigma_C \frac{N_e N_{ph} F_{rep}}{2\pi(\sigma_e^2 + \sigma_{ph}^2)}, \tag{1}$$

where N_e and N_{ph} are the numbers of electrons per bunch and the number of photons per laser pulse respectively, $\sigma_C \sim 6.65 \times 10^{-17}$ μm^2 the Compton cross section, σ_e and σ_{ph} the root mean square (rms) of the transverse dimension of the two incident beams (assumed to be Gaussian) at the IP, and F_{rep} the repetition frequency of the interaction. To calculate the expression Eq. (1), incident beams are assumed to have identical horizontal and vertical dimensions and to collide head-on. The flux formula for the general case can be found in [10].

From the kinematic of the Compton process, the energy E_X of a scattered photon in the laboratory frame can be written as

$$E_X = \frac{2\gamma^2 E_L(1 - \cos\theta_i)}{1 + \gamma^2\theta^2}, \tag{2}$$

TABLE I. ThomX design parameters.

Parameter	Value	Units
Electrons		
Gun injection frequency	50	Hz
Ring revolution frequency	16.67	MHz
Bunch energy	50–70	MeV
Bunch charge	1	nC
Laser		
Optical cavity frequency	33.3	MHz
Laser wavelength	1.03	μm
Energy per pulse	21	mJ
Stored laser power	0.7	MW
Interaction point		
Incident angle	2	°
Electron spot size (rms)	70	μm
Laser spot size (rms)	40	μm
Electron bunch length (rms)	25	ps
Laser pulse length (rms)	10	ps

where $\gamma = E_e/m_e c^2$ is the electron Lorentz factor, m_e and E_e the electron mass and energy, c the speed of light, E_L the energy of the incoming photon, θ_i and θ, respectively, the incident angle and the scattering angle with respect to the electron direction. To derive expression Eq. (2), it was assumed $\gamma \gg 1$ and $E_L \ll m_e c^2$. In Compton interactions, there is an univocal dependency between the energy of a scattered photon and its scattering angle. Photons emitted in the forward direction (at the so-called Compton edge) have the maximum energy.

The nominal parameters of ThomX (summarized in Table I) are $F_{rep} = 16.67$ MHz, $N_e \sim 6 \times 10^9$ (1 nC per bunch), $N_{ph} \sim 10^{17}$ (21 mJ per pulse), $\sigma_e \sim 70$ μm and $\sigma_{ph} \sim 40$ μm, resulting in a total flux of $\sim 10^{13}$ x-rays/s expected in the energy range 45–90 keV (on axis), a transverse source size of ~35 μm, and an average brightness of 10^{11} ph (s mm^2 mrad^2) in 0.1% of bandwidth. X-rays are produced in the electron beam direction and are transported through a vacuum beam pipe to an experimental X-hutch located after the concrete wall of the bunker (see Fig. 1). The angular aperture available for the x-ray beam is constrained by the mechanics of the optical cavity that delimits a maximum opening half-angle of 7 mrad. Details of the ThomX machine can be found in [11,12].

This article aims to present the first results of the ThomX commissioning that began in summer 2021, as soon as the French Nuclear Safety Agency (ASN) gave its authorization. In 2021, ThomX was authorized to operate the straight line of the injector; in 2022, to send the electron beam in the transfer line, the ring, and the extraction line; and finally in 2023, to send the x-ray beam in the experimental X-Hutch. In this publication, we provide a comprehensive description of the physical parameters for each subsystem in dedicated sections. Where applicable, we compare these parameters

with numerical simulations to highlight the correspondence with the design. Commissioning of the injector, transfer and extraction lines, ring, laser system, synchronization system, diagnostic devices, and x-ray line is detailed in Secs. II–VI. Then the first production of high-intensity x-rays is presented (Sec. VII).

II. INJECTOR

The objective of the ThomX injector is to produce electron bunches, accelerate them, and guide them toward the ring with the good matching conditions of the Twiss parameters for ring injection and optimization of the orbit. The injector, illustrated in Fig. 2, comprises three primary sections: a photoinjector, a transfer line, and an extraction line.

The photoinjector consists of a 2.5 cell radio frequency gun (rf gun), designed like the CTF3 model [13]. The rf gun features an 80 MV/m accelerating gradient, providing a 5 MeV energy gain, and includes a solenoid for emittance compensation [14,15]. This solenoid is composed of two coils: one functions as a focusing magnet at the exit of the rf gun, while the other is designed to neutralize the magnetic field at the photocathode. After the gun, a linear accelerating section of "Linac Injector of LEP" (LIL) type [16] on loan from Synchrotron SOLEIL [17] provides a 45 MeV energy gain, with maximum on-axis field of 14 MV/m, elevating the electron beam to 50 MeV. The gun and the LIL section are fed by an rf power network.

In the transfer line, four primary dipoles bend the beam, while seven quadrupoles focus it. An injection dipole adds 169 mrad to the trajectory for ring injection, and five steerers correct the horizontal and vertical orbit. When the injection dipole is switched off, the beam can travel into the extraction line without passing through the ring. The beam from the ring is ejected in the extraction line and transported toward the final dump at the repetition frequency of the Linac (50 Hz). The extraction line includes an extraction dipole with 169 mrad deflection (switched off for ring extraction, and switched on for direct extraction), seven quadrupoles, two dipoles, and two steerers.

Various diagnostics are employed to characterize the electron beam in the injector (see Sec. IV): three integrated current transformers (ICT) for beam charge measurements, five YAG screen stations for beam size measurements, and six stripline BPMs for position measurements.

During the initial commissioning phase, the Linac generated electron bunches at a frequency of 10 Hz, each carrying a charge of 100 pC and an energy of 50 MeV.

A. rf power network

The rf power network is mainly used to transport and distribute the rf power from a modulator-klystron (type E37310 from Toshiba) to the standing-wave gun and the LIL traveling wave accelerating section by means of a network of rectangular oxygen-free high conductivity copper WR284 waveguides and other rf components, such as bidirectional couplers, a power divider, rf loads, rf windows, a circulator, variable attenuators, and a variable phase shifter. The position of such devices in the network layout is shown in Fig. 3. The whole network is stabilized at temperature of $24 \pm 1\,°\mathrm{C}$ (to avoid length variation in the waveguides due to different operating conditions) and pressurized at 2.5 bars relative to atmosphere with sulfurhexafluoride (SF6). rf ceramic windows are used to transmit and separate the rf power between the pressurized and the vacuum regions. The klystron delivers 37 MW peak output power with a variable rf top pulse width of up to 4.5 μs and a maximum repetition rate of 50 Hz. As illustrated in Fig. 4, the rf power is divided into two channels by a power divider. On the side, which runs toward the electron gun, a variable attenuator is installed to change the transmitted power. In addition, there is a circulator to protect the klystron from the reflected rf power that occurs at the rise and fall edges of the rf pulses or in case of internal discharges (rf breakdown) in the gun. On the other side, which transports the power toward the

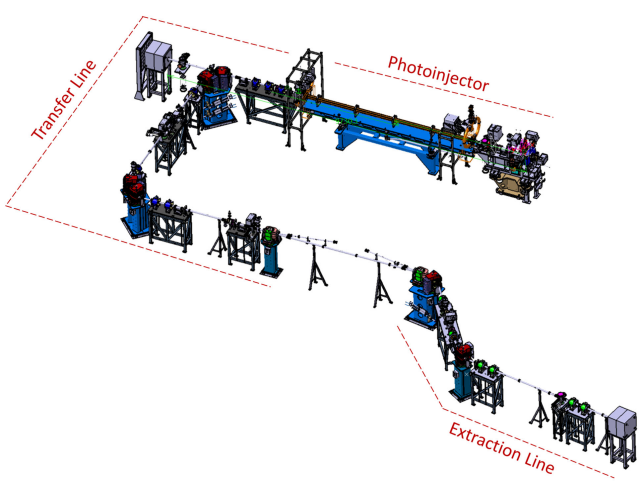

FIG. 2. View of the ThomX injector.

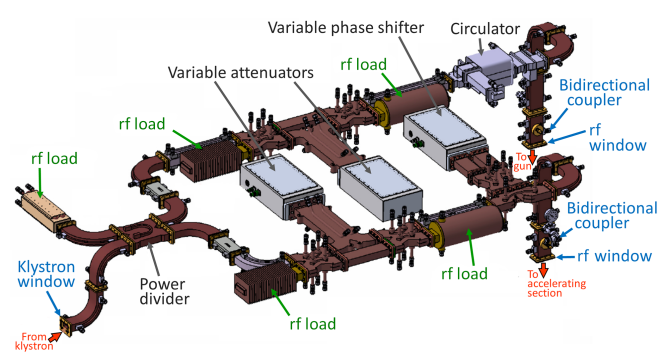

FIG. 3. 3D drawing of the ThomX power distribution network and rf components.

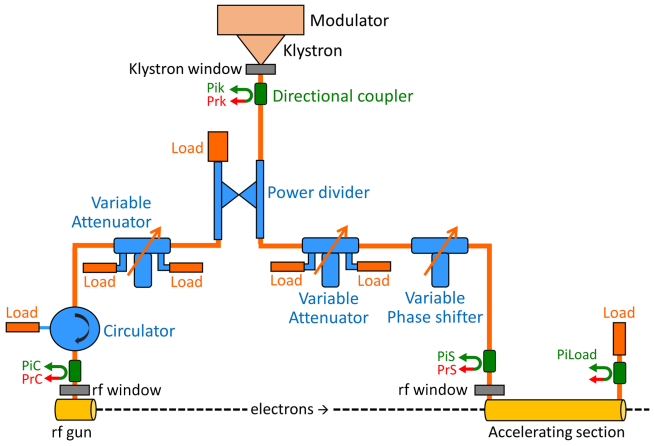

FIG. 4. Diagram of ThomX power distribution network. Pik, Prk, PiC, PrC, PiS, and PrS are the incident (i) and reflected (r) rf powers of the klystron (k), gun (C), and section (S), respectively, and PiLoad the residual rf power at the section output. In operation, these quantities are measured continuously.

accelerating structure, there is also a variable attenuator that varies the transmitted power, and a phase shifter to adjust the relative rf phase between the gun and the accelerating section. For incident and reflected power measurements, four couplers are installed in this network. The first is located at the klystron exit, the second at the rf gun entrance, and the last two at the entrance and exit of the accelerating section (see Fig. 4).

B. Electron beam production from the gun

1. Photocathode laser

A subpicosecond fiber oscillator operating at a wavelength of 1030 nm and a repetition frequency of 41.64 MHz is succeeded by a regenerative amplifier (the "s-Pulse HP2" from Amplitude Company) along with a fourth harmonic generator. The resulting laser system outputs a UV pulse with an energy around 200 μJ at a wavelength of 257 nm, a pulse repetition ranging from 1 to 50 Hz, and a tunable pulse width between 4 and 9 ps (full width at half maximum) at 1030 nm. The laser is connected to the accelerator through a transport line spanning approximately 20 m, consisting of a series of dielectric mirrors. In proximity to the Linac, a breadboard is installed, featuring a tunable iris and a telescope that transmits the iris image onto the cathode. Transverse laser profiles at different iris apertures from 1 to 3.5 mm are presented in Fig. 5. The temporal and transverse shapes of the laser pulse, together with the quantum efficiency of the photocathode surface, determine the temporal and transverse distributions of the electron beam upon emission. The nonuniformity of laser spatial distributions, clearly visible in Fig. 5, is likely due to a nonoptimal transport of the laser until the cathode and will have a significant impact on the electron beam distribution. The measured asymmetry on the horizontal

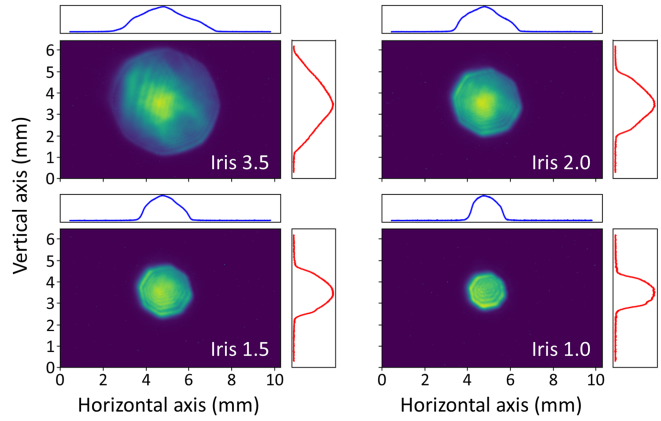

FIG. 5. Laser transverse intensity distributions and horizontal and vertical projections along the center lines, taken at different iris apertures.

and vertical laser transverse profiles, shown in Fig. 6, will be also transferred to the electron beam.

For ThomX operation, the iris aperture was set to a diameter of 1.3 mm, corresponding to a laser spot size of around 0.35 mm (rms).

2. Characterisation of the beam from the gun

Comprehensive beam characterization from the rf gun was undertaken, beginning with the measurement of the charge against the rf gun phase as depicted in Fig. 7. The rf gun phase is defined there as the phase relationship between the rf electromagnetic wave coupled into the gun and the laser impacting the photocathode. It is a critical parameter governing the tuning of energy, emittance, and energy spread in the accelerator. The charge was measured using an ICT (see Sec. IV) positioned 0.9 m after the cathode subtracting the dark current. The measurements follow the standard for such a 2.5 cell rf gun with a phase

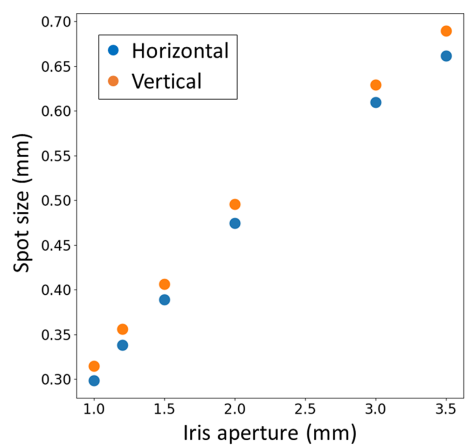

FIG. 6. Laser transverse beam size (statistical rms) measurements as extracted from projections on horizontal and vertical axes, as a function of the iris aperture.

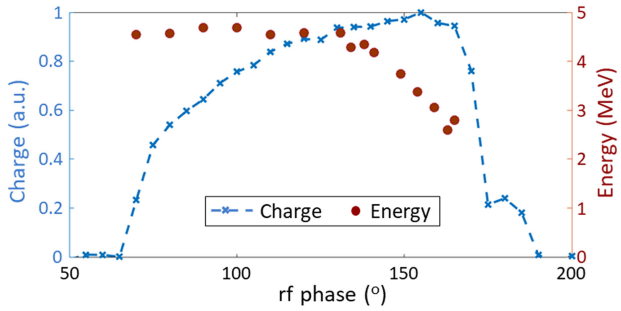

FIG. 7. Charge and kinetic energy measured at the exit of the rf gun versus its rf phase. The energy measurements were provided by a steerer and a screen spaced by 0.77 m.

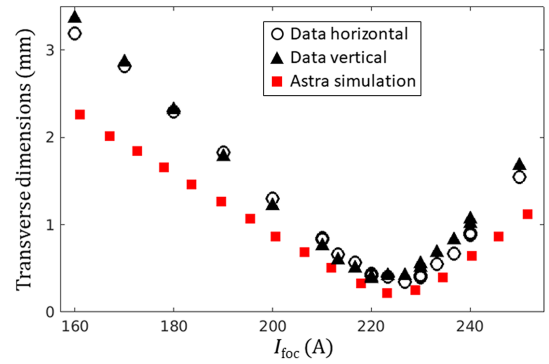

FIG. 8. Horizontal and vertical beam sizes (statistical rms) at the gun exit measured with a YAG screen at 1.2 m from the cathode compared with ASTRA simulations versus the focusing solenoid current. A factor of 0.9 have been applied to simulated values of I_{foc} (see text).

span of approximately 100°. The observed charge increases until a maximum value, whose behavior is attributed to the well-known Schottky effect [18]. Then, the charge abruptly decreases. Without an available spectrometer at the gun exit, energy measurement involves correlating the beam position at a YAG screen (see Sec. IV) with the magnetic field properties of a steerer magnet. The phase yielding the maximum energy is offset by 50°–60 ° (a value contingent on the accelerating gradient) from the one maximizing charge. This phase difference arises from the inherent slippage between the electron and the electromagnetic wave, a consequence of the nonrelativistic velocities at the cathode, and the subsequent acceleration to relativistic speeds over a distance of approximately 12 cm, as discussed in [19]. The rough adjustment of the phase is done daily using the charge phase measurement, while the energy measurement is used occasionally to confirm the rf accelerating gradient.

The alignment of the laser and the solenoids has been done as described in [20]. Then, the beam size versus focusing solenoid current, I_{foc}, was measured using a removable YAG screen placed at 1.2 m from the cathode and compared with ASTRA simulations [21]. To obtain a zero field at the cathode, the current values in the two solenoids are linked according to a known relation [22]. For the measurements, the current in the second solenoid was adjusted to the focusing one according to this relation. From the simulations and the measurements, we have extracted the statistical rms of the horizontal and vertical beam sizes for each value of I_{foc}. Results are shown in Fig. 8. The behavior of the measured beam sizes is well reproduced by the simulations, although there are some disagreements between the two: on the one hand, the measured sizes are higher than simulated sizes and, on the other hand, the simulated values of the solenoid current had to be shifted by a factor of 0.9 in the figure to match the location where the size is minimal. These discrepancies may be due to the fact that the two solenoids were not measured experimentally prior to installation. As a result, the dependence of the magnetic field on the current in each of the solenoids may be slightly different from that predicted in the design [22], and a nonzero field may be present at the cathode location. This issue will be investigated in the near future.

C. Characterisation of the beam at 50 MeV

From the gun exit, the 100 pC electron beam is fully transmitted in the transfer line through the accelerating section over a large span of solenoid values, from 160 to 230 A.

1. Transverse beam size

When the field of the two first 45° dipoles is at zero, the beam is directed to the beam dump. At this location, the beam's size and position can be measured using a removable YAG screen placed at 3.2 m from the exit of the LIL just before the dump. The tuning of the solenoids, so focusing on the accelerating section entrance is crucial since it will drive the performances in terms of emittance for the ring injection.

Using the YAG screen, the beam size versus focusing solenoid current has been measured and compared with ASTRA simulations. Results are shown in Fig. 9 where, as in Fig. 8, the same factor of 0.9 has been applied to simulated solenoid currents. For these measurements, the three quadrupole magnets at the LIL output were switched off and, for the simulations, a drift space was considered between the LIL section and the YAG screen. The order of magnitude of the beam sizes is well reproduced by the simulation but shows disagreement for values of I_{foc} lower than that corresponding to the minimum beam size. This is not yet understood. It could be due to a too simple simulation of the LIL section or, here again, to the effect of a nonzero magnetic field on the cathode. This question will be investigated.

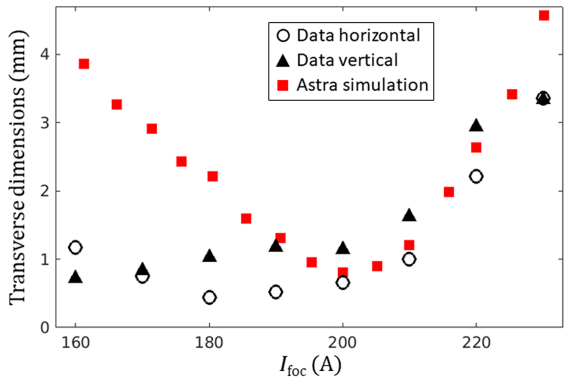

FIG. 9. Beam size (statistical rms) measured at 3.2 m from exit of the LIL section with a YAG screen, compared with ASTRA simulations, versus the focusing solenoid current. A factor of 0.9 has been applied to simulated values of I_{foc}.

2. Emittance measurement

The quad scan technique, a standard method for measuring beam emittance, is adapted to the ThomX injector configuration. Beam emittance is derived from a series of beam sizes obtained during a quadrupole scan using the thick lens approximation, as detailed in [23].

For further insight into the implementation of this technique, beam dynamics simulations with the ASTRA code [21] were performed from the photocathode to the YAG screen, including emittance measurement simulations with the quad scan. Thereafter emittance obtained from the quad scan simulation is denoted as "simulation-measured" emittance to distinguish it from experimentally measured one, while emittance calculated by ASTRA from second-order moments of particle distributions in phase space is denoted as root mean square (rms) emittance.

There is a consistent correlation between "simulation-measured" emittances and rms emittances, over a wide range of quadrupole strength scan for a beam with a Kapchinsky-Vladimirsky-like distribution [24,25], while at the Linac exit, for the beam distribution originating from particles emitted by a photocathode and accelerated in rf fields, the "simulation-measured" emittance values are aligned with rms emittance only within a narrow quadrupole strength scan range near the minimum beam waist on the screen. Over a broad scanning range, the "simulation-measured" emittance can exceed the rms emittance by an order of magnitude, as the fitted parabola deviates significantly from the minimal beam size squared. Analyses indicate that the beam exhibits an open-fan-like particle distribution in transverse phase space due to the time-dependent forces of space charge and the radial components of the rf field. Under these conditions, the beam's phase space distribution cannot be precisely depicted by an ellipse based on the second central moments of particle statistics. Thus it is crucial to choose a range where the beam size squared on the screen closely matches a parabolic function of quadrupole strength.

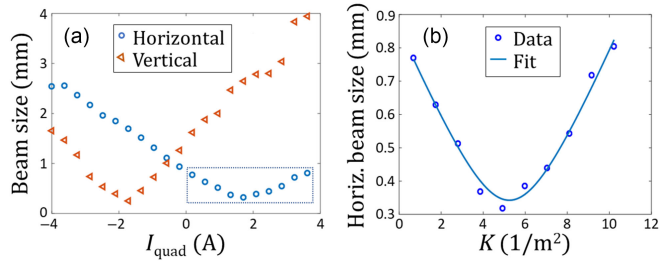

FIG. 10. Example of experimental quad scan at focusing solenoid current of 215 A (a) and scan processing to obtain beam emittance (b), which was found equal to 1.3 π mm mrad. The fitted line represents the square root of a parabolic fit of the squared beam size. I_{quad} is the quadrupole current, and K the quadrupole strength.

On the other hand, if conditions for the conservation of the volume occupied by particles in 6D phase space are fulfilled according to Liouville's theorem, the conservation of the area of this volume's projection onto the 2D phase plane occurs only when there is no particle energy spread and no correlations of particle positions in phase space (see, for example, [26]). Indeed, the simulation of the quad scan showed that rms emittance did not remain constant for a beam from the Linac. It is almost constant only for a narrow range around the beam waist on the screen. Therefore, it is preferable to measure beam emittance at the Linac exit using only one quadrupole to avoid influences of others on the beam.

Considering the above, we conducted multiple sets of emittance measurements using the third quadrupole for scanning. From the projected profile of the beam's image on the screen, we utilized the full width at half maximum (FWHM) as a more reliable indicator of the beam size, rather than the rms value derived from a Gaussian fitting. Figure 10(a) illustrates an example of these measurements, where each FWHM beam size was calculated as the average of five successive beam images captured for each quadrupole current value. Figure 10(b) shows the result of the quad scan processing by using data from Fig. 10(a) lying within the dotted square.

When fitting, we have obtained an emittance value of 1.3 π mm mrad (rms). To obtain this rms value from FWHM measured values, the relation rms $=$ FWHM$/2.36$ was used on the beam sizes. This is an approximation since the distributions are not Gaussian.

Quadruple scans were carried out for several values of solenoid currents, successively to ensure the same conditions of the Linac. Data were processed as mentioned above to deduce each rms emittance value. Results are presented in Fig. 11. The figure also includes simulated emittances. In these simulations, to be close to the ThomX operating value, the beam is accelerated from a copper photocathode illuminated by a laser with a spot size of 0.35 mm (rms) in both horizontal and vertical directions.

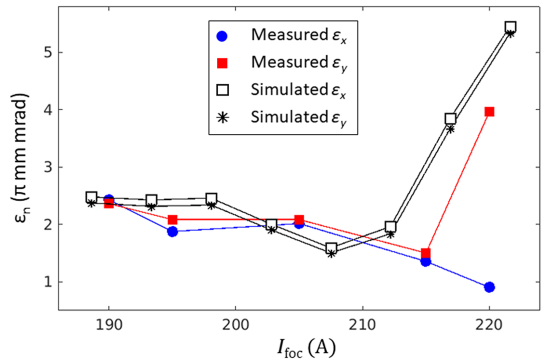

FIG. 11. Normalized emittances (rms) from experimental quad scans and simulated normalized rms emittances versus solenoid current. The lines are shown to guide the eye.

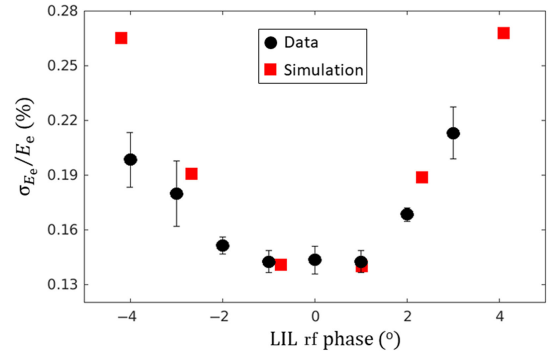

FIG. 12. Energy spread (statistical rms) of the 50 MeV, 100 pC beam deduced from the beam sizes on the YAG screen after the first two dipoles of the transfer line, as a function of the rf phase of the accelerating section, and comparison with ASTRA simulations.

Most probably, the small differences between simulated horizontal and vertical emittance values visible in Fig. 11 are caused by the low particle statistics, as the Linac field maps were axially symmetric. There is a reasonable correlation between the measured and simulated data. The significant disparity between the measured horizontal and vertical emittances at 220 A is likely due to the asymmetry of the laser spot. With a focusing solenoid current of 220 A, the measured beam spot on the YAG screen positioned between the rf gun and the entrance to the accelerating section appears as an ellipse rotated approximately 45° clockwise from the vertical axis, indicating that the motions in the horizontal and vertical planes are interconnected, which may influence emittance measurements.

As quadrupole scanning emittance measurements are very sensitive to the nonuniformity of the particle distribution in the phase space, nonuniformity of the photocathode laser's transverse distribution (see Sec. II B 1) can lead to nonuniformity and an increase in both emittance measurement errors and real beam emittances.

3. Energy spread measurement

The relative phase between the electromagnetic wave inside the rf gun and the laser impinging the cathode is driven by the synchronization system of the Linac (see Sec. VI). To tune independently the phase between the rf of the gun and the rf of the LIL accelerating section, a motorized phase shifter was installed on the rf branch of the LIL section (see Sec. II A).

To measure the energy spread, we used the two first 45° dipoles of the transfer line as a spectrometer. The beam was focused with the three quadrupoles Q1, Q2, and Q3 located just after the exit from the LIL section. The horizontal position on a YAG screen located 2.2 m after the dipoles was converted into kinetic energy. The contributions coming from the beam's transverse size and beam divergence were neglected, which is a reasonable assumption. The energy spreads were then deduced from the transverse profile of the images. Results of measurements and ASTRA simulations are presented in Fig. 12. With optimal tuning of the phase of the rf gun and of the LIL section, a minimum energy spread of 0.14% was measured for a beam with 50 MeV energy and 100 pC charge. The error bars on measurements in Fig. 12 come from shot-to-shot variations.

D. Electron beam transport to the ring

As shown in Fig. 2, the transfer line does a U-turn with four dipoles. It transports the beam from the exit of the LIL accelerating section to the ring injection point. The solenoid and the seven quadrupole currents have to be tuned to match the optics between the injector and the ring. Three quadrupoles (Q1, Q2, and Q3) are located at the exit of the LIL, two others (Q4 and Q5) between the two pairs of dipoles, and the last two (Q6 and Q7) in the straight line before the ring injection point.

Knowing beam emittance enables the derivation of Twiss parameters, which are crucial for transporting the beam through the transfer line into the ring. Figure 13 presents the result of the β and α function evaluations at the entrance of the third quadrupole for both measurements and simulations. While there is a fairly good agreement between the measured and simulated emittance (the ellipse's area in the phase plane divided by π) as it is depicted in Fig. 11, the

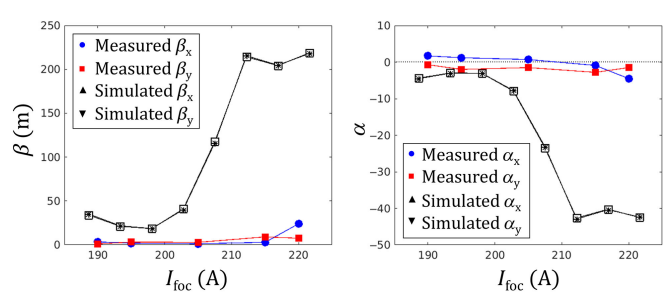

FIG. 13. Experimentally measured and simulated Twiss parameters β (left) and α (right) versus focusing solenoid current. The lines are shown to guide the eye.

ellipse's shape and orientation defined by the β and α functions are significantly different. This discrepancy suggests that the Linac model used for single particle dynamics simulation does not accurately reflect the actual setup. For example, besides, a much higher β function at solenoid currents higher than 200 A, the simulation shows that for all mentioned solenoid current settings, the beam is strongly focused within the accelerating section, causing it to diverge at the entrance of the third quadrupole. In contrast, measurements indicate that while the beam always diverges in the vertical plane, it converges in the horizontal plane when the solenoid current is at or below 205 A (see Fig. 13, right plot). Simulations that included random variations in accelerator parameters did not show a trend that would reduce the discrepancy between measured and simulated results at solenoid currents higher than 200 A. Furthermore, beam image processing errors cannot explain the large discrepancy either. This suggests the need for further investigation.

The low measured values of the β function (Fig. 13, left plot) cause problem of beam transportation through the transfer line because it was designed for a divergent beam with an initial beta function of 40 m [11]. Hence, the transfer line lattice was recalculated with the MadX code [27] for a solenoid current of 220 A, initial β of 18 m, and α of -3 to match beam parameters at the ring injection point. A set of quadrupole currents was thus obtained, then empirically adjusted during the ring injection process based on the following considerations: (i) By slightly modifying the electron beam energy, the orbit dispersion at the ring entrance should be equal to half the orbit dispersion measured between the two pairs of dipoles. (ii) The beam should be as round as possible on the YAG screen located before the injection point. (iii) The beam should have a minimum size on the YAG screen located between the two pairs of dipoles.

After these adjustments, the beam was transported through the transfer line without loss (at a solenoid current of 220 A). The values for the currents of the quadrupoles Q1, Q2, and Q3 were very close to the simulated ones, those of Q4 and Q5 slightly different, and those of Q6 and Q7 quite different. Dedicated transfer line studies should be carried out to understand the model-machine correspondence.

III. STORAGE RING

A. Ring layout

The ThomX Storage Ring (SR) layout is shown in Fig. 14. It is a compact (17.986 m total circumference) 50 MeV ring employing a Double Bend Achromat optics with a twofold symmetry. There are eight 45° dipoles for a complete turn achievement and 24 quadrupoles to shape and focalize the beam. The SR also has 12 sextupoles for chromaticity corrections and 12 correctors integrated with the sextupoles for both the horizontal and the vertical planes to correct the orbit. The SR vacuum chamber is made of stainless steel and has an elliptical shape with an aperture of 40 mm in horizontal by 28 mm in vertical plane. Figure 15 shows the nominal optical functions along the ring. Nominal horizontal and vertical tunes are 3.17 and 1.64, respectively. Momentum compaction factor is 0.014.

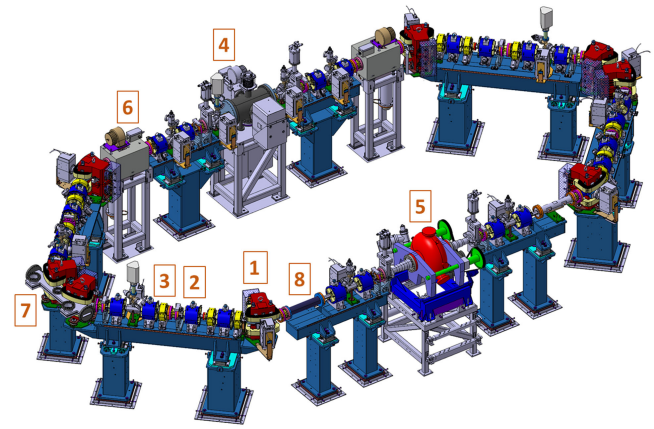

FIG. 14. ThomX storage ring layout. Shown in the figure are 1: 8 dipoles (red), 2: 24 quadrupoles (blue), 3: 12 sextupoles (yellow), 4: septum, 5: rf cavity, 6: 2 kickers (injection/extraction), 7: IP chamber, and 8: feedback transverse stripline.

An on-axis on-momentum injection scheme was chosen for the storage ring: the electron bunch from the Linac and transfer line is injected into the ring after final deflection provided by an eddy-current septum magnet and then a fast (injection) dipole kicker. Once the electron beam is deemed no longer viable for Compton scattering (after 20 ms according to the nominal design), it is extracted to a beam dump first by a kick provided by a fast (extraction) dipole kicker and then by the eddy-current septum magnet that

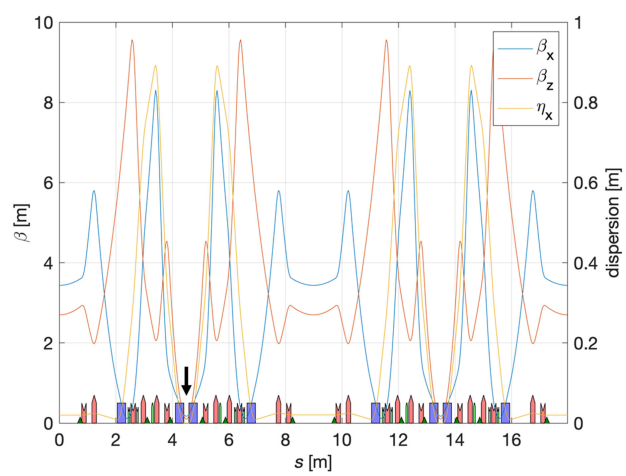

FIG. 15. ThomX storage ring nominal optics: horizontal beta function (blue), vertical beta function (red), and horizontal dispersion (yellow). Black arrow indicates the IP.

was used as well for injection. A description of the mechanisms by which electron beam quality is degraded is given later in this subsection. All three pulsed magnets are installed in one dedicated straight section of the ring with link to the injection and extraction transfer lines. The pulsed systems were designed and specified by the SOLEIL pulsed magnet team and built by SigmaPhi in Vannes, France.

The eddy-current septum magnet is of a traditional and rugged design. It provides a horizontal beam-stay-clear of 7 mm between the septum blade and the stored beam axis in the storage ring as well as a distance of 15.5 mm from that axis to the injected or extracted beam axes [28]. The vertical aperture is the same as for the rest of the machine, i.e., 28 mm. The magnet is powered by a resonant capacitive discharge pulser equipped with a fast thyristor and precision charging power supply. The delivered current pulse is bipolar sinusoidal with a pulse duration of and a peak current of roughly 1500 A, required for the beam up to 70 MeV. The system operates up to 50 Hz repetition rate with a reproducibility of the peak current pulse better than 0.1%.

The injection and extraction kicker magnets share the same design. A ceramic vacuum chamber is coated with a thin layer of titanium that must be thick enough to minimize impedance and beam induced heat load, while thin enough to allow the pulsed magnetic field to enter the chamber and deflect the beam. Two small kicker magnets are installed around the chamber. The electrical connections have been improved to minimize parasitic inductance. For qualitative injection or extraction of the electron bunch, it is critical that both the rise and the fall of the pulsed magnetic field be less than one revolution. This means the pulsers must deliver half-sine current pulses no larger than 120 ns (i.e., two turns) with a peak current that can reach 800 A peak for the 70 MeV electron beam. The design of the kicker pulsers differs from the usual topologies. Traditionally, kicker systems require the shortest coaxial transmission possible between the pulser and the magnet. With short transmission, with respect to the pulse wavelength, the coaxial cable inductance adds to the magnet's, and this leads to smaller energy storage capacitor and usually higher voltage on the pulser components and on the magnet itself. In that case, one can neglect the current wave propagation. However, when the transmission line is significantly larger than the pulsed current wavelength, it is possible to dissociate the behavior of the pulser from what occurs when the current reaches the magnet. In the case of ThomX, the kicker pulsers are resonant capacitive discharge in which the capacitor (few nanofarads) oscillates on the pulser parasitic inductance and the coaxial line impedance. The generated pulse travels through the transmission line up to the magnet. The magnet is of low impedance compared to the transmission line impedance and, according to transmission line theory, the current in the load can be as much as doubled, given the mismatch in impedance.

As ThomX is a machine dominated by nonlinear dynamics, commissioning and operating the ring is a major challenge owing to high particle density and low-energy operation, mismatched beam injection, absence of damping (much larger than the 20 ms of storing time), strong effect of coherent synchrotron radiation, intrabeam scattering (IBS) and Compton backscattering (CBS), and other collective effects including the ion instabilities and ring impedance [11,29–33]. The beam dynamics in the ThomX ring differ significantly from those in conventional synchrotron storage rings. A longitudinal mismatch of the injected bunch combined with strong coherent synchrotron radiation induces a transient microbunching regime that persists for several tens of microseconds [32,33]. This transient behavior leads to beam losses and an increase in transverse emittance, particularly at higher charges approaching 1 nC. Hence, longitudinal and transverse feedback systems are indispensable for the beam stability. Longitudinal bunch shaping is ensured by an ELETTRA-type cavity, operating at 500 MHz (30th harmonic of the ring frequency), and powered by a 40 kW SOLEIL-type solid-state amplifier. The longitudinal feedback system allows the damping of the longitudinal oscillation during 20 μs (about 300 turns). The transverse feedback is made of a dedicated stripline installed at one of the long straight sections (see Fig. 14) to provide 5 μs damping time. Over longer timescales (∼ms), collective effects such as IBS and CBS further influence the beam dynamics resulting in additional beam losses, increased transverse emittance, and energy spread. This evolution cannot be stopped since there is no short-term damping with ThomX's electron and laser beam parameters. Indeed, taking into account the laser's radiative cooling [5] and the effect of synchrotron radiation, both transverse and longitudinal damping times are of the order of a second [11,29,30], much greater than the 20 ms of the storage time. This absence of significant damping makes the stored electron bunch highly susceptible to these collective effects causing the x-ray production rate to decrease rapidly during beam storage. Simulations indicate that, at ThomX, the x-ray flux decreases by a factor of around 2 over the 20 ms storage period.

Ring diagnostics are based on 12 beam position monitors (BPM). These monitors, described in Sec. IV B, provide the beam position information for both single pass data and turn-by-turn data averaged over two turns. In addition, there are beam loss monitors and synchrotron radiation monitors (see Secs. IV E and IV D).

B. Commissioning

The expected final total alignment errors of the assembled SR components are about 100 μm in each plane. The survey performed before the beam commissioning phase showed alignment errors less than 80 μm (rms)

measured for quadrupole and dipole magnets. Authorization from the ASN for the commissioning of the transfer line, storage ring, and extraction line was obtained under the same conditions as for the initial phase (10 Hz injection repetition rate, an electron bunch charge, and energy up to 100 pC and 50 MeV, respectively).

After successful injection and beam threading phase, by doing the orbit correction, we achieved beam storage for more than 300 turns in the ring without powering the rf cavity (see Fig. 16). Beam storage was further improved by beam tuning, chromaticity corrections, scaling the quadrupoles [34]. As injector beam parameters were not always stable and varied from shift to shift, to optimize and facilitate injection search, we applied the robust conjugate direction search (RCDS) method [35]. In order to maximize the objective function, which is in our case the sum of turn-by-turn BPM sum signals from all electrodes for the first and last BPM in the ring, a set of seven parameters is varied by RCDS, among which are two pairs of transfer line correctors (horizontal and vertical), injection dipole, septum, and kicker currents. In less than 15 min, with 500 iterations of the algorithm, we found systematically optimal injection parameters.

After the rf cavity and its systems were commissioned, we began to scan the cavity rf feed frequency in a narrow range around its design value and the field phase over a range of 2π to capture the injected bunch in the ring separatrix [36]. For nominal optics configuration (i.e., for momentum compaction factor, α_c, equal to 0.014), these attempts ended in failure, so a measurement scheme was prepared to find the free rotation frequency of the bunch around the ring. The scheme consisted of a mixer to which the sum signal from the beam position monitor electrodes in the ring, passed through a bandpass filter with a central

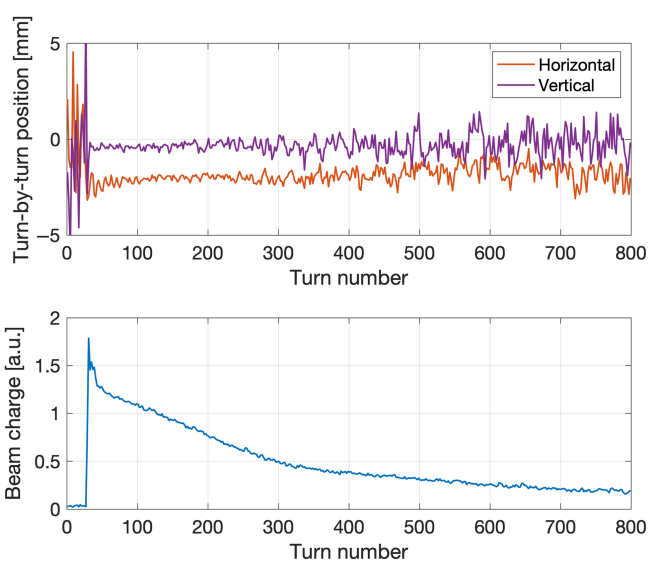

FIG. 16. First beam storage: turn-by-turn beam position (top) and charge measured by a ring BPM (bottom).

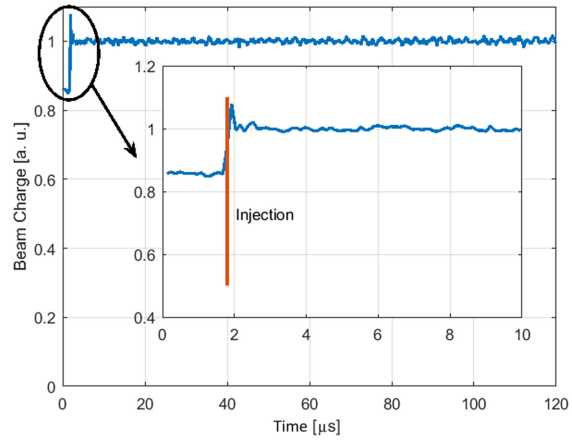

FIG. 17. Beam storage in the ring over 0.12 ms at the rf frequency of 500.38 MHz. An inset provides a close-up view of the first 10 μs of the storage process.

frequency of 500 MHz, and the excitation signal from the ring cavity were fed. The study of the signal at the output of the mixer showed that the 30th harmonic of the bunch-free rotation frequency is higher than the nominal one from 300 to 400 kHz, depending on the energy of the injected beam. After setting the rf cavity to a frequency within this range, beam storage was obtained at cavity voltage up to 100 kV (see Fig. 17). Measurements of closed orbits during the frequency search process to obtain the nominal operation are shown in Fig. 18. In an attempt to store the beam at a lower rf cavity frequency, beam loss occurred at frequencies lower than 500.27 MHz.

The first beam physics studies have been performed showing a good agreement with the SR model (see Fig. 19). Routinely, during the operation, the horizontal tune was measured to be 3.17 corresponding to the nominal value. A vertical tune was measured via the vertical-to-horizontal coupling to be 0.91 (fractional part) being higher than the

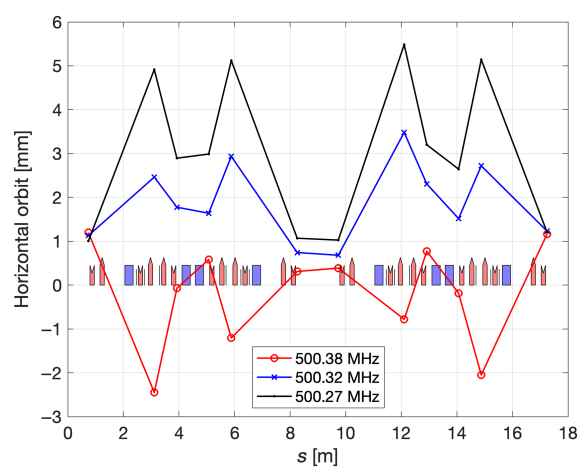

FIG. 18. Horizontal closed orbit measurements conducted during ring commissioning. The beam loss occurs below 500.27 MHz for the nominal optics configuration.

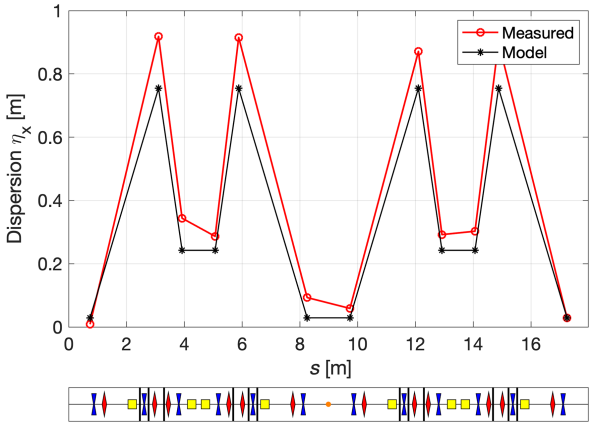

FIG. 19. Measured horizontal dispersion for the nominal optics configuration compared to the model dispersion calculated at the BPM locations.

nominal value of 1.64. It should be noted that thanks to the heterodyne synchronization scheme of the bunch injection into the ring, it was possible to obtain an injection in approximately the same rf phase on each trigger (see Sec. VI). However, the stability of the bunch injection phase is an issue that requires improvement for the current synchronization scheme.

As the rf frequency was found to be higher than the nominal one, this resulted in the impossibility to synchronize the electron bunch circulating in the SR with the laser pulse circulating in the Fabry-Perot cavity (see Sec. V) since the laser frequency range is limited to 500 ± 0.27 MHz. Hence,

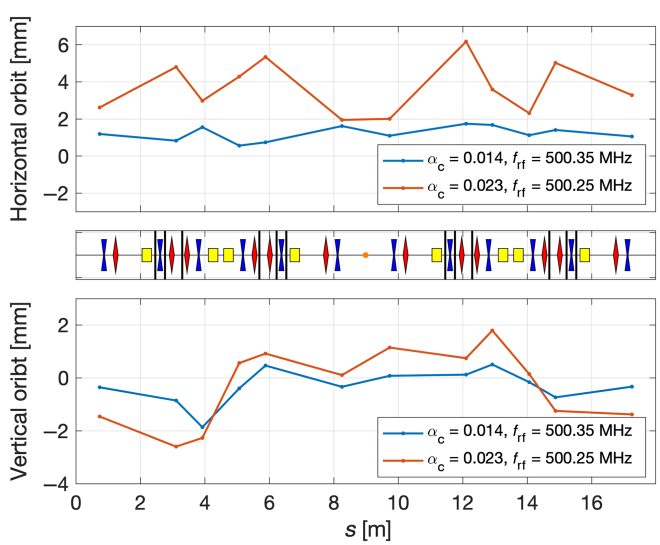

FIG. 20. Closed orbit measurement at 500.25 MHz with new optics featuring a higher momentum compaction factor ($\alpha_c = 0.023$) compared to the closed orbit measured with nominal optics ($\alpha_c = 0.014$) at a natural frequency of 500.35 MHz. Operation on the dispersive orbit at 500.25 MHz is developed temporary to enable synchronization between laser pulses and circulating electron bunch.

a temporary solution based on new optics with a higher value of the momentum compaction factor (being 0.023 instead of 0.014) was implemented, allowing beam storage at 500.25 MHz on the dispersive orbit (see Fig. 20). While such constraint on the circumference is not typical in standard storage rings, it is a fundamental issue in energy recovery linacs (ERLs). Possible solutions in ERLs include implementing an orbit bump in an arc [37] or using movable tables to adjust the positions of magnets [38].

C. Current status

We established several working points of the SR operation including the nominal lattice and a temporary lattice with a higher momentum compaction factor to operate the SR at 500.25 MHz to be able to synchronize with the Fabry-Perot cavity. Extensive studies were carried out to understand the reason for the higher ring revolution frequency (i.e., shorter circumference) than the nominal one. Theoretical and experimental investigations were made to understand the physical origins of this mismatch. These studies included beam-based alignment, mechanical alignment, dispersion measurements, searches for beam storage at other ring frequencies and dipole currents, as well as direct measurements of the beam revolution frequency. Simultaneously, beam tracking simulations were performed using a realistic dipole fieldmap that was both simulated in OPERA [39] and experimentally measured. Two approaches were employed: slicing the dipole magnets in the Accelerator Toolbox code [40] and explicitly incorporating the dipole fieldmap into the ring model in the rf-track code [41]. Studies with both methods have shown that the beam trajectory in the dipoles is shorter with respect to the ideal path, due to dipole fringing field, resulting in the shorter path length and smaller total SR circumference. The ThomX dipoles, which have a bending radius of 0.377 m at 50 MeV, are C-type magnets with two coils wound around the magnet yoke near the poles. Despite the coil dimensions (40 mm in width and 60 mm in height), the coils protrude approximately 70 mm into the drift space between the dipole poles and the adjacent beam optics elements of the ring. Combined with the magnet gap of 42 mm, this configuration creates a long fringing field compared to the magnet length, contributing to the observed effect. We investigated possible ways to compensate for dipole fringing fields and retrieve nominal frequency: displacement of the dipoles; adding metallic plates around the dipoles to reduce fringing field; and mechanical extension of the ring by about 12 mm. This last method is the most promising and the least disruptive in terms of installation and mechanical integration. Moreover, beam optics studies have shown that nominal ring parameters could be conserved together with the recovery of nominal operating rf frequency. This mechanical intervention is planned in 2024. In the meantime, the operation of the ThomX SR at the higher value of

momentum compaction factor has been prepared and used for the synchronous x-ray production. Finally, the longitudinal and transverse feedback systems are installed and will be commissioned *in situ* in the nearest future.

IV. DIAGNOSTICS OF THE ELECTRON BEAM

The following types of diagnostics are installed all along the machine to measure the beam properties: (i) Beam profile monitors (screen stations); (ii) beam position monitors (BPM); (iii) integrating charge transformers (ICT); (iv) Faraday cups (FC); (v) visible synchrotron radiation monitors; and (vi) beam loss monitors (BLM).

Their location on the machine can be seen in Fig. 21. They have been described in detail in [28].

A. Beam profile monitors (screens)

Beam profile monitors are installed in five different locations on the machine (see Fig. 21). They are described extensively in [42]. They consist of a motorized arm on which are installed screens. A picture of the profile monitors stations (called screen stations) is shown in Fig. 22(a). The ultrahigh vacuum (UHV) compatible motorized arms are 150-mm-long standard linear shift (LSM38-150-SS) made by UHV Design. A set of screens is installed at the tip of the motorized arm as shown in Fig. 22(b): a calibration target (USAF 1951), a YAG:Ce screen, an aluminum screen, and a sapphire screen (specific to the station in a straight line from the Linac).

The outermost of these screens is a UHV-compatible USAF 1951 patterned wheel target (from Edmund Optics) used to measure the resolution and the magnification of the optical system. An automated software has been written to measure the resolution and magnification automatically [43]. For all stations, it has been verified that the resolution is better than the specification of 100 μm. Next, there is a YAG:Ce screen manufactured by Crytur with a diameter of 25 mm and a thickness of 0.2 mm. The choice of YAG:Ce

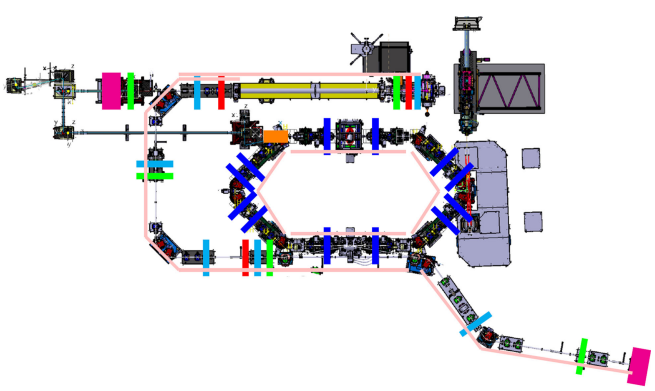

FIG. 21. Position of the beam diagnostics in ThomX [28]. Light blue: stripline BPM; dark blue: button BPM; green: screen station; red: ICT; dark pink: FC; light pink: BLM; and orange: visible synchrotron radiation monitor.

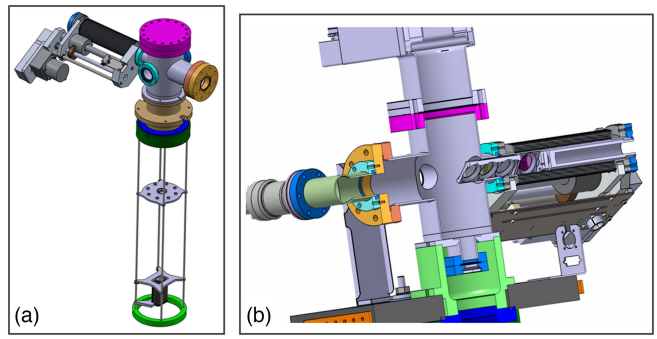

FIG. 22. (a) Overview of the screen stations in which the profile monitors are installed. The UHV compatible motorized arm is visible on the left, the imaging camera is shown below. On the top of some stations, a vacuum pump is installed. (b) Cut view of the center part of a screen station. Four screens can be seen at the tip of the motorized arm, from left to right: calibration target (USAF 1951), YAG:Ce screen, aluminum screen, and sapphire screen.

was made to ensure a good light yield, even at a low beam charge. The third screen is an aluminum foil used to generate optical transition radiation (OTR) to measure the beam profile at a high charge without blooming. All these screens are titled with an angle of 45° with respect to the beam axis so that the light produced is directed downward toward a camera. At one of the stations, the one located in a straight line from the Linac, there is in addition a Sapphire screen (also from Crytur) with a diameter of 25 mm and a thickness of 0.3 mm. This screen is used to produce Cerenkov radiation that is then transported to a streak camera to measure the pulse length (under commissioning). An example of image from each of these four screens is presented in Fig. 23. All screens, but the

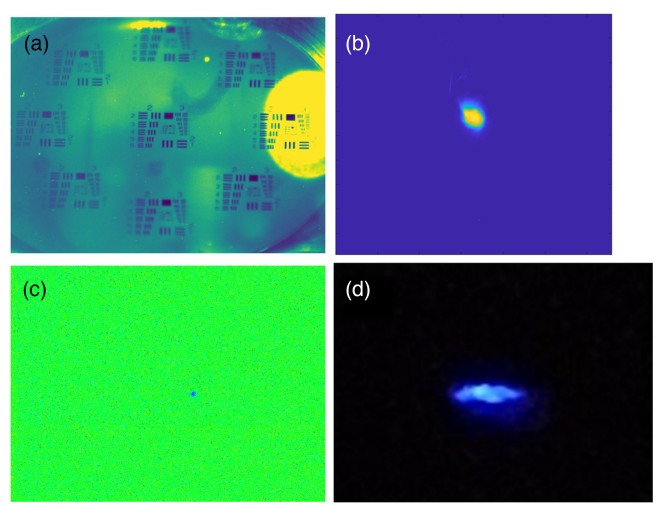

FIG. 23. Image of (a) an USAF 1951 target, (b) the light emitted by a YAG:Ce screen, (c) the light emitted by an aluminum foil used as OTR screen, (d) the Cerenkov light emitted by the Sapphire screen. Images were taken on the screen station at the end of the Linac.

sapphire one, are imaged from below by an imaging camera. An LED system is used to illuminate the target screen when resolution measurements are done.

B. Beam position monitors

Two types of BPMs are used: stripline BPMs in the straight lines and button BPMs in the ring. They have been built in-house, except for the electrical feedthrough, which has been purchased commercially. Their position is shown in Fig. 21. The signal is transported outside the accelerator bunker by long cables with phase pairing for the four electrodes, then read by Libera Brilliance+ modules from instrumentation technologies. Noise measurements have been made on each electronic module as part of the acceptance test. The single pass accuracy on the beam orbit is expected to be better than 500 μm, and better than 200 μm for the ring turn by turn. Using slow acquisition, we expect to reach an accuracy better than 200 μm. Numerical simulations have been used to estimate the response of the BPMs and thus their calibration. This calibration has been cross-checked on a test bench for one BPM [44] and a network analyzer has been used to measure the position offset and electrodes coupling (including the response of the cables).

C. Charge monitors

The beam charge is measured in several places along the beam orbit using integrated current transformer and Faraday cups. There are three ICTs and two FCs (see Fig. 21). The analog signal is transported out of the ThomX bunker with low losses cables and then digitized using a Wavecatcher digitizer [45] developed in-house.

The ICTs (procured from Bergoz, model ICT-CF6”-60.4-40-UHV-070-5.0) provide a charge-to-signal ratio of 1/10 with an accuracy of 0.5% according to Bergoz calibration data. Cable losses are estimated to be 10%. The waveform is measured over 1024 samples. Based on the noise performances of the wavecatcher, the expected noise is around 15 pC (rms), compatible with the noise observed during machine measurements. A future improvement will be the reduction of the integration gate, which is proportionally linked with charge equivalent noise. One can divide by three the integration gate length, aiming a charge noise below 7 pC (rms).

The FCs are installed within the beam dumps: one at the end of the Linac and the second one at the end of the extraction line. FCs are based on the design made for the SOLEIL Faraday Cups and beam dumps, scaled to the lower energy of ThomX. They are made of a block of graphite connected to a wire. A filter is installed on the wire at the exit of the dump to match the cable’s impedance (50 Ω). As the signal width after filtering is longer than the memory depth of the wavecatcher, the charge measurement obtained is proportional to the total charge. It is not an absolute measurement.

D. Visible synchrotron radiation monitors

As illustrated in Fig. 21, a window has been installed on one of the dipoles of the ring to monitor the beam size using visible synchrotron radiation. However, this wavecatcher system is not yet in operation and will be commissioned in the nearest future.

E. Beam loss monitors

Two types of BLM are installed and used at ThomX: fiber beam loss monitors (FBLMs) and scintillator detectors.

FBLMs offer an appealing beam loss diagnostics tool. They work by detecting the electromagnetic shower generated by beam losses via Cherenkov radiation emitted by the charged particles within the multimode fibers attached to the vacuum chamber. Subsequently, this radiation is converted into an electrical signal, which contains information about the position and intensity of the beam losses [46]. The fiber used at ThomX is manufactured by LEONI Fiber Optics GmbH. It belongs to the Hard Plastic Clad Silica (fibers category. These fibers feature a fused silica glass core, 630 μm of optical cladding made from polymer, and a 950 μm Tefzel jacket. To detect the Cherenkov light, the fiber is coupled with a photon detector (the photosensor module H10721-01 manufactured by Hamamatsu Photonics) containing a PMT and a built-in high-voltage power supply circuit. In total, seven different fibers are installed along the entire accelerator: one on the Linac, one on the transfer line, one on the extraction line, and four to cover the entire storage ring. Within the storage ring, the FBLM has been installed in four sections so that losses from different turns can be separated.

In addition to the FBLM, a compact BLM based on a CsI (Tl) scintillator (8 by 10 mm) coupled to a PMT (the same model as used for the FBLM) has been developed. The full scintillator assemblies are affixed to the vacuum chamber. These additional BLMs are installed at specific locations (injection/extraction, Linac, transfer line on request, etc.) to provide additional information alongside the FBLM, while it is being calibrated to ensure precision in beam loss locations.

BLM signals acquired during the commissioning phase are depicted in Fig. 24. The signal shown in Fig. 24(a) comprises a slow-time component, reflecting the scintillation process within the crystal. Additionally, two fast spikes at the beginning of the red waveform are more likely to originate from direct photoemission in the PMT photocathode generated by the electromagnetic shower. The emergence of the second spike served as compelling evidence of the successful completion of the first turn in the ring during its commissioning phase. Notably, electromagnetic interference induced by the injection kicker is prominently evident in the waveforms. The signal from the storage ring FBLM is visible in Fig. 24(b): the peaks

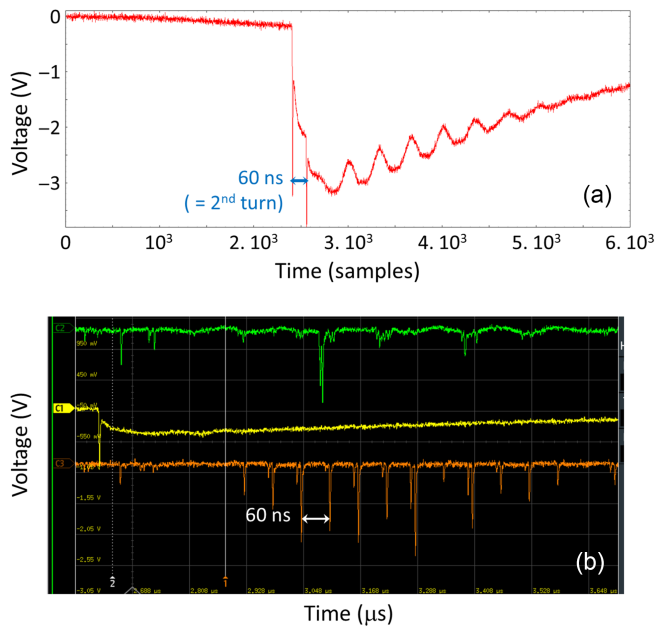

FIG. 24. BLM signals recorded during the ring commissioning phase. (a) Scintillator signal at injection: the waveform depicts the signal captured by the scintillator detector installed at the septum for monitoring injection losses. (b) Oscilloscope screenshot displaying the signal from the storage ring FBLM (in green and orange) along with the scintillator signal (in yellow).

observed at regular intervals of 60 ns correspond to turn-by-turn losses within one of the storage ring arcs.

Overall, the commissioning and use of the BLM at ThomX have met expectations. It offered valuable insights, particularly during the initial stages of the ring commissioning, aiding in the search and optimization of injection and beam storage processes.

V. FABRY-PEROT CAVITY SYSTEM

To produce the nominal ThomX x-ray flux, the optical system has to generate an intense photon beam that must be precisely positioned and synchronized with the electron bunch circulating inside the ring. The laser wavelength was chosen at 1030 nm (1.24 eV), enabling the achievement of the required x-ray energy [45–90 keV for electron energy of 50–70 MeV, see Eq. (2)]. Besides, this choice allows the use of high-average power "chirped pulse amplification" (CPA) technology based on Ytterbium doped gain media. The laser beam source is thus composed of a low-power and ultrastable oscillator, coupled to a powerful fiber laser amplifier delivering around 100 W of average power. However, the CPA amplification scheme is unable to provide the performances of Table I. To reach the 700 kW regime of laser beam average power, one is forced to use, in addition, an optical resonator (i.e., a Fabry-Perot cavity) [47].

As depicted in Fig. 25, the full laser system and the optical cavity are mounted on a table located at the

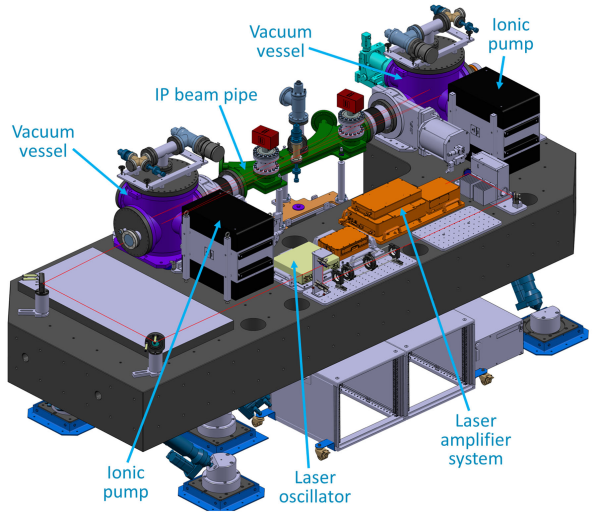

FIG. 25. The Fabry-Perot cavity system. The principal elements on the granite table: in yellow the laser oscillator, in orange the laser amplifier system, in purple the two vacuum vessels holding the cavity mirrors, in green the IP beam pipe, and in black the ionic pumps.

Compton IP. The optical table consists in a massive granite slab to ensure thermal and mechanical stabilities. The slab is mounted on a six degrees of freedom hexapod (from Symétrie Company) to align the laser beam onto the electron beam with micrometric precision. The optical table is surrounded by a thermal and vibration isolating housing similar to previous experimental setups [6,7]. Eventually, a laminar airflow, covering the entire system, is used to prevent dust contamination when operating on the optical system.

The rest of this section is devoted to a description of each component of the optical system represented in Fig. 25 and its commissioning.

A. The optical setup

The optical setup is described in detail in [48,49]. A 33.3 MHz laser oscillator (Origami from NKT/Onefive Company), that is twice the electron bunch frequency, delivering pulses of 186 fs (FWHM) of the intensity profile and 44 mW average power is used. This is a low-phase noise oscillator as required for a high-finesse cavity seeder. Figure 26 shows phase noise measurement of our oscillator (see [50] for technical details) together with one of our reference continuous wave (cw) oscillators (from OEwaves Company). The corresponding residual integrated temporal jitters are shown in Fig. 27. However, a residual integrating jitter below ≈0.01 fs is mandatory for seeding our 9 m long and 30,000 finesse cavity (i.e., 1.1 kHz frequency linewidth). From Fig. 27, one can then infer that a feedback bandwidth around 100 kHz must be supplied.

The laser fiber amplifier system is provided by Alphanov Company. Its architecture [49] is similar to those described

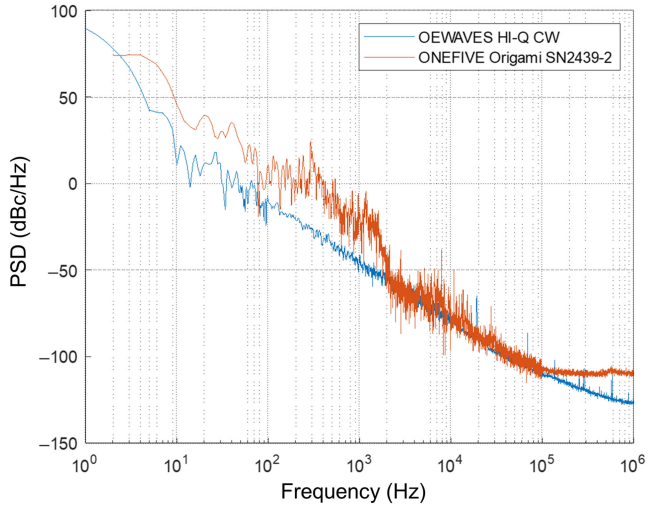

FIG. 26. Measurement of the power spectral density of phase noise at the optical frequency (291, 262, and 136 MHz) with an ultrastable cw laser as a reference oscillator, from OEwaves company.

in [48,51]. The pulses are chirped up to approximately 1 ns (FWHM) after the oscillator using Chirped volume Bragg grating (CVBG) [52], then amplified by three stages Yb doped fibers before being recompressed by two CVBG. The final pulse duration is measured by an optical autocorrelator. Assuming a sech^2 envelop intensity profile, we obtain 8.4 ps FWHM [49] (that is 4.8 ps rms). The compressor efficiency is found to be around 70%. The average output power of the fiber amplifier system (after pulse compression) can be tuned in the range from a few watts up to 70 W. The phase noise added by the amplifier was not noticeable.

A telescope made of four lenses is implemented after the amplifier in order to match the laser beam shape with the cavity fundamental mode [51].

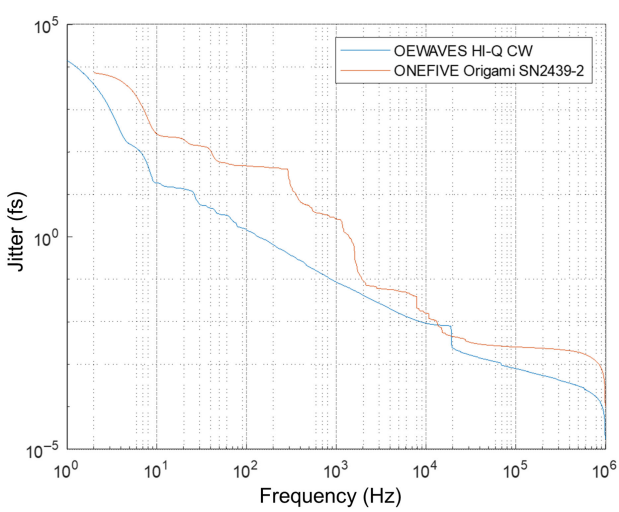

FIG. 27. Measurement of the equivalent integrated temporal jitter of the two laser oscillators used for Fig. 26.

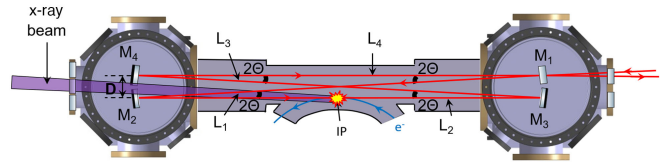

FIG. 28. Schematic drawing of the Fabry-Perot cavity. M_2 and M_3 are the two spherical mirrors and M_1 and M_4 the two planar mirrors. The optical axis (bow-tie shape) is also shown, together with the beam axes incident and reflected by M_1. Design values of the other geometrical parameters: the incident angle of the optical axis on the cavity mirror surfaces $\Theta = 21$ mrad, $D = 9.5$ cm, $L_1 = L_3 = 2.2509$ m, $L_2 = 2.2502$ m, and $L_4 = 2.2475$ m.

The geometry of the optical resonator is shown in Fig. 28. This is a planar bow tie cavity, made of two planar (M_1 and M_4) and two spherical (M_2 and M_3) 1 in. diameter mirrors. This geometry allows the laser beam to be focused between the two spherical mirrors, with the repetition rate to be independently maintained and matched to the ring rf frequency by adjusting the distance in between the two planar mirrors [53]. All mirror mounts include two motorized tilt angle and one longitudinal actuators similar to those of [7] (see [48] for details). The laser beam is injected inside the resonator though M_1. Each pair of mirrors M_1, M_3 and M_2, M_4 are located in vacuum vessel cylinders. These cylinders are connected to the electron beam pipe by a dedicated mechanical piece (see Fig. 29) allowing the laser beam to enter it through a 0.8×6.5 cm slit.

The substrates of the spherical mirrors have a radius of curvature of 2.241 m (before coating). Figure 30 shows the calculation [47] of the laser beam transverse sizes along the cavity optical axis. With our cavity geometry, and assuming perfect mirror surfaces, the waist size of the fundamental mode between the spherical mirrors is expected to be around 130 μm for both sagittal and tangential directions (i.e., a waist of 65 μm rms for the laser beam intensity profile).

Figure 31 shows a measurement of the laser transverse beam profile behind M_4. However, the measured ellipticity and its orientation are not those expected from Fig. 30. We checked by simulations that this discrepancy cannot be explained by a nonplanar optical path inside the cavity [54]. Nevertheless, it could be explained by a slight deformation of the cavity mirror surfaces (e.g., by adding a radius of curvature of 115 m to M_4 orientated by 45), which could originate from an imperfect polishing or mounting constraints. Simulations taking into account this assumption predict a smaller collimated beam in the constraint direction leading to a more elliptical beam on the mirrors with a size of 2.85 mm × 2.09 mm (as shown in Fig. 31), and a waist size of 130 μm × 170 μm between the spherical mirrors.

To achieve storage of laser pulses in the optical cavity and produce a power gain of the order of 10,000, highly reflective mirrors with minimal absorption and diffusion losses are required. This was obtained by specific coating

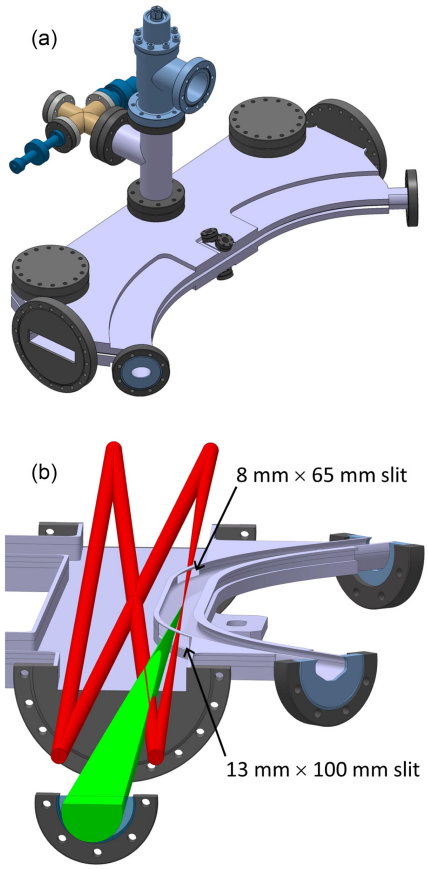

FIG. 29. Drawings of the IP chamber of ThomX. (a) Top view of the chamber and (b) schematic of the beam path, in red the laser beam and in green the produced x-ray beam.

runs at the LMA Laboratory leading to a mirror coating absorption loss of about 0.5 ppm and a residual diffusion loss of a few ppm. High-purity layer coating was also achieved in order to reduce the presence of hot spots [55,56]. As for the mirror substrates, we followed [57] by using low absorption fused silica for M_1 and ultralow expansion (ULE) material for the other mirrors. This is an optimal choice for reducing the mirror thermoelastic deformations budget in the high-average power regime.

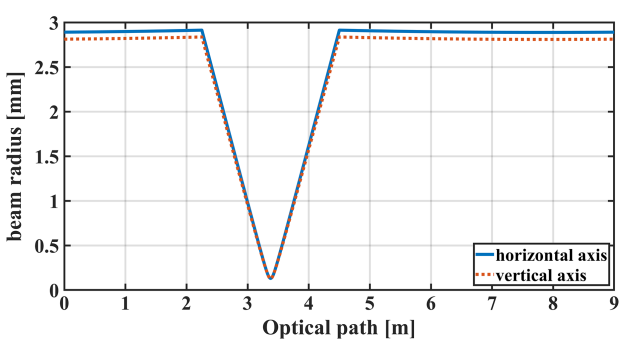

FIG. 30. Transverse size calculations of the cavity fundamental mode as a function of the longitudinal position along the optical axis.

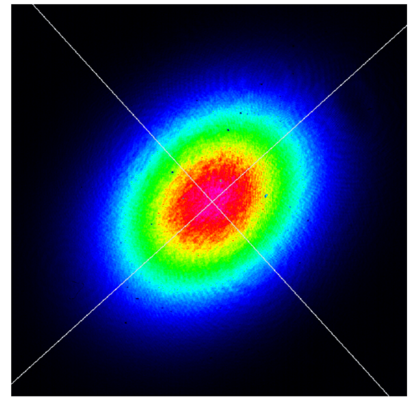

FIG. 31. Transverse intensity distribution of the fundamental mode stored in the cavity, measured at 10 cm behind M_4. The beam radii are 2.85 and 2.09 mm along the minor and major axes of the elliptic profile.

The cavity finesse was initially measured during the installation of the mirrors using our reference continuous laser oscillator (from OEwave, see Fig. 26 for its phase noise spectrum measurement) and the method of [58]. We obtained a finesse value of around 30,000, from which a power gain of approximately 10,000 was inferred [51]. During the ThomX commissioning phase, a stack average power of ~90 kW, measured behind M_4, was maintained stably inside the optical cavity. Such a high optical power concentrated on surfaces of a few square millimeters induces mirror deformations [59], which in turn induces high order modes (HOM) degeneracy that leads to laser-cavity locking instabilities [60]. To address this issue, a movable mechanical arm, holding a L-shape metal component was installed to spatially filter out these HOM (see Fig. 32), which have a larger spatial extension than the fundamental mode [61].

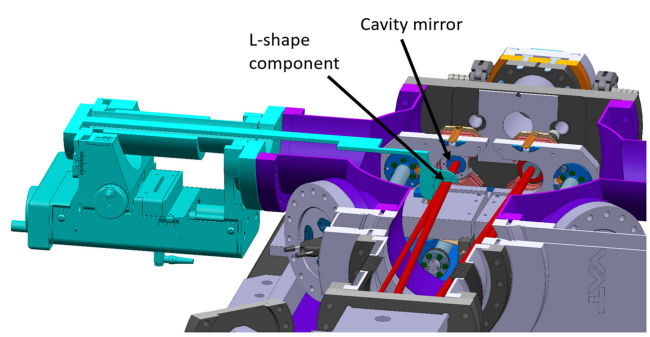

FIG. 32. 3D-view of the mechanical arm holding the L-shape metallic piece in front of a mirror. The arm is moved manually in the vertical plane along two directions. The arm mover is located outside the cavity vacuum vessel (see the cyan colored system on the left part of the drawing). Mirror mounts are also visible, and the optical axis of the cavity mode is also schematized for the sake of clarity.

B. Fabry-Perot cavity locking

To operate the optical resonator, the optical system requires two synchronization systems: (i) A fast feedback control loop of the laser oscillator cavity length (based on the Pound-Drever-Hall technique [62]) to compensate for any drift of the arrival times of the laser pulses relative to those already stored inside the optical cavity. (ii) A slow feedback control loop of the length of the Fabry-Perot cavity to prevent any drift in the relative timing between the laser pulses and the ring rf master clock (see Sec. VI).

The two feedback control loops are schematized in Fig. 33. They rely on a commercial equipment (TEM-Messtechnik Laselock device) that enables the implementation of two channels digital Proportional-Integral-Derivative (PID) controllers. The loop that controls the laser beam repetition frequency acts on two elements implemented inside the laser oscillator: a piezoelectric quartz via the digital PID and an electro-optic crystal via a fast analog gain loop. This loop reduces the temporal jitter between the oscillator and the cavity. The loop that controls the length of the Fabry-Perot cavity relative to the 500 MHz frequency of the ring reference clock (corresponding to the 15th harmonic of the laser oscillator's repetition frequency) only acts on an annular piezoelectric quartz attached to one of the cavity planar mirrors through the digital PID. The measured rms residual jitter regarding the 500 MHz clock is about 3–4 ps, compatible with the length of the electron bunch.

In order to maximize the average power stacked inside the cavity, the carrier-to-envelop phase (CEP) pulse-to-pulse drift of the laser beam is tuned manually using a dedicated actuator located inside the laser oscillator. As shown in [8], even with picosecond laser pulses, a detuned CEP leads to a power drop inside high-finesse cavities. In this case, with our setup, we measured an average power loss above 90%. Fortunately, once optimized, the CEP was changing very slowly during the cavity operation. Hand tuning was therefore enough to keep an optimum average power inside the cavity.

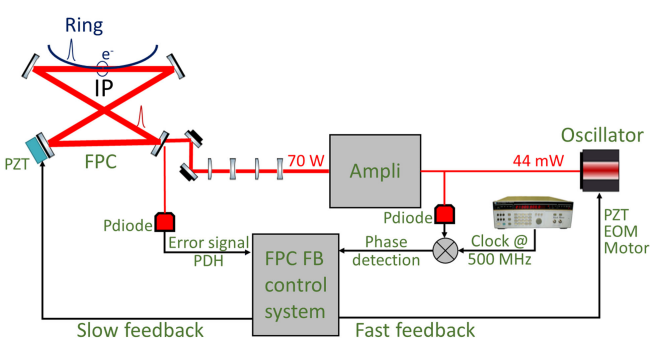

FIG. 33. Simplified scheme of the optical setup and block diagram of the two feedback control loops. "FPC" means fabry-perot cavity, "FB" feedback, "PDH" pound-drever-hall, "PZT" piezoelectric transducer, "EOM" electro-optical modulator, and "Pdiode" photodiode.

C. Perspectives

Operating the optical cavity with only 90 kW of stack average power was justified by the following facts: (i) Risk mitigation of mirror destruction induced by hot spot defects located inside the mirror coatings, as we experimented in earlier experiments [55]. (ii) Prolonged operation at this relatively low power will help clean the surface of the optical cavity mirrors and allow for a gradual increase in cavity power with minimal risk of breakage. (iii) Higher average power was not required during the commissioning phase aiming to debug all machine components.

In the future, for ThomX operations, the laser amplifier power will be increased from the current 16 up to 70 W, and the coupling will be improved by a dedicated telescope design. With these improvements, a stacked average power of around 500 kW is foreseen inside the optical cavity. Up to now, 600 kW has been obtained [57] with a higher incident laser beam power, and more recently, the stacking of 550 kW stable average power was demonstrated in a high-finesse four-mirror bow-tie cavity [63] with 75 W of incident power. Besides, stable stacking of 720 kW in a two-mirror cavity setup has recently been reached with mirrors originating from the same coating batch as those used for the present work [64]. All the technological bricks are then in place to reach stable average power stacking around 500 kW in a near future.

VI. SYNCHRONIZATION SYSTEM

The synchronization system has two functions: it distributes low-power rf signals to all systems that need rf signals and controls the time at which each equipment of the machine is triggered with respect to a reference time. To ensure that the elements are triggered at the correct phase, the trigger signal occurs when there is an heterodyne coincidence between all rf signals, hence fixing their phase relationship. The rf signals involved are the following: (i) low-level rf (LLRF) for the gun and the LIL accelerating cavitiy (see Sec. II), operating at the LIL frequency [16]: 2998.55 MHz; (ii) low-level rf for the ring cavity (see Sec. III) operating around 500 MHz; (iii) the oscillator of the photocathode laser (see Sec. II B 1) operating at 41.64 MHz; and (iv) the oscillator of the interaction laser (see Sec. V) operating at 33.3 MHz.

In addition to these rf signals, several devices need to receive trigger signals at an appropriate time to perform their function. During the design phase, the option of operating the Linac and the ring at strict harmonics of each other (2998.55 MHz and 499.76 MHz) was considered, but it was felt that the seasonal variation of the ring's length might drive the gun and the Linac outside their frequency

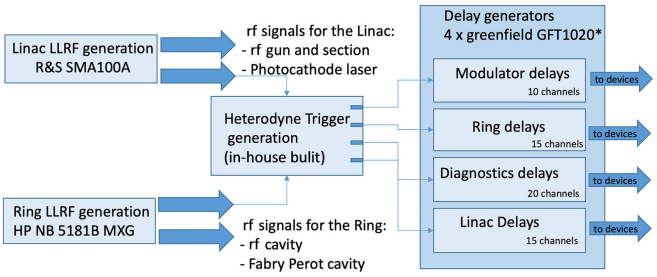

FIG. 34. Block diagram of the ThomX synchronization system.

acceptance. It was thus decided not to operate at harmonic frequencies. This led to the development of a coincidence detection system based on heterodyne beating between all the frequencies used in ThomX. The heterodyne trigger generation system, named triggerbox, was built in-house and is described in Sec. VI C. Qualification tests of such system on another project are described in [65] and led to the development of the synchronization scheme [66].

The ThomX synchronization system must achieve the following performances: (i) a synchronous operation of the main power (50 Hz); (ii) a jitter between the Linac rf signal and the photoinjector laser less than 1° (rms) relative to the Linac frequency; (iii) a jitter between the ring rf and the Fabry-Perot laser less than 1° (rms) relative to the ring frequency; (iv) a jitter between the ring rf and the Linac rf (divided by 6, i.e., 499.76 MHz) at injection such as 90% of the shots are within 4° at 500 MHz; (v) a jitter between trigger signals and heterodyne coincidence less than 100 ps (rms).

A block diagram of the overall synchronization system is shown in Fig. 34. The signal synthesizers for the Linac LLRF and the ring LLRF were chosen with ultralow-phase noise: for the Linac, it is a Rohde & Schwarz SMA100A, for the ring, a Hewlett Packard NB 5181B MXG. The distribution of the LLRF signals for the Linac and the ring is described in Secs. VI A and VI B, respectively. Four delay generators presented in Sec. VI D distribute the trigger signal to all the machine devices.

A. Linac LLRF generation

The Linac LLRF system delivers the rf signal that is then amplified by the modulator-klystron (see Sec. II A) to feed the electron gun and the accelerating section. Its frequency is 2998.55 MHz. A triggered switch limits the delivery of this signal to the amplification chain to only a few microseconds per trigger. A second branch of this signal is divided by 6 in frequency to provide the reference frequency (499.76 MHz) for the photocathode laser (this reference frequency is further divided by 12 inside the laser). A phase shifter is placed between these two branches to allow a fine control of the phase of the rf in the electron gun with respect to the laser pulse arrival. This scheme is presented in Fig. 35.

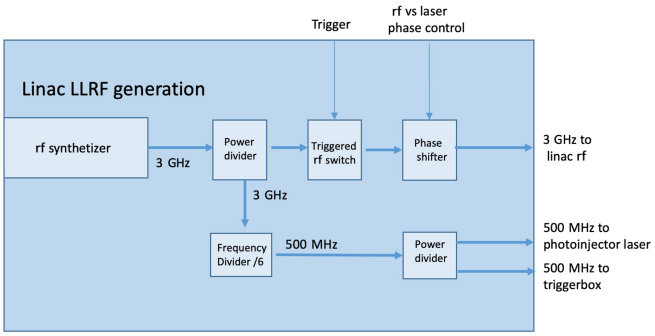

FIG. 35. Block diagram of the linac LLRF distribution scheme.

B. Ring LLRF generation

The ring LLRF generation provides the reference frequency to the ring. This frequency is fixed by the ring size to about 16.67 MHz. Two devices are using this frequency: the rf ring cavity (described in Sec. III) operating at 500 MHz (30th harmonic of the ring frequency), and the Fabry-Perot optical cavity (described in Sec. V) operating at 33.3 MHz (15th harmonic of the ring frequency). As the Fabry-Perot cavity is not permanently locked to the ring LLRF, it was decided to reconstruct a stable 33.3 MHz for synchronization stability. Due to the long lead time on procuring a divider by 15, the LLRF signal sent back to the heterodyne trigger generation uses (temporarily) a separate synthesizer linked to the ring LLRF synthesizer by a 10 MHz link. This scheme is presented in Fig. 36.

C. Heterodyne trigger generation

Due to the constraints discussed above, the Linac and ring frequencies are not harmonics of each other. To ensure a fixed phase relation between the Linac and the ring frequencies, the trigger signal is generated when there is a heterodyne coincidence between them. To ensure that all devices are in the correct phase, both the lowest and highest frequencies of the Linac and ring branches are used in the heterodyne mixing. These frequencies are coming from the

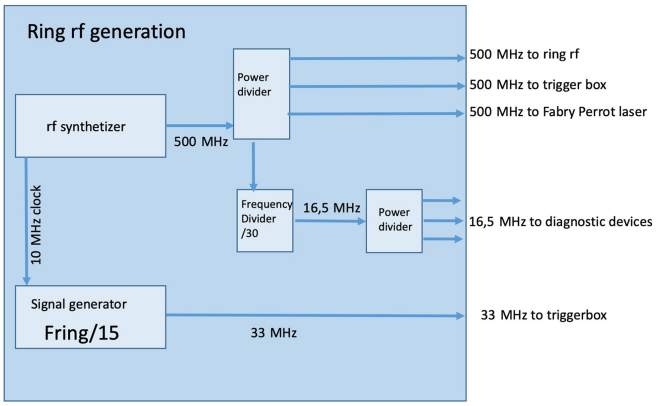

FIG. 36. Block diagram of the ring LLRF distribution scheme.

Linac LLRF synthesizer (divided by 6: 500 MHz) and from the photocathode laser (41.64 MHz) for the Linac branch, and from the ring LLRF synthesizer directly (500 MHz) and divided by 15 (33.3 MHz) for the ring branch. The two 500 MHz signals are mixed together to provide heterodyne beating between the Linac and the ring; however, this beating does not freeze the phase of the photocathode laser and Fabry-Perot cavity (33.3 MHz) signals. Further processing is done using a complex programable logic device (CPLD) with fast comparators converting analog input signals to signals suited to the CPLD. In the CPLD, the photocathode laser and the ring 33.3 MHz signals are used to create gates that restrict the choice of heterodyne coincidences from the 500 MHz mixer to only those at a fixed phase of the photocathode laser and the ring 33.3 MHz signal. This gated beat signal is further gated to be at a fixed phase of 50 Hz from the main electrical power network. After passing all these gates, the pulses are sent to counters that will send a trigger signal at the required submultiple of 50 Hz. The diagram explaining how this works is shown in Fig. 37.

It should be noted that this scheme only works if there is at least a small difference in frequency between the Linac divided by 6 frequency (typically 499.76 MHz) and the ring frequency (nominally 500.02 MHz, typically 500.30 MHz). We expect this to be always the case with the frequencies used at ThomX.

D. Delay generators

The delay generators are used to distribute trigger signals to all devices requiring one. They have been purchased from Greenfield technology and are derived from their GFT1020 product but with a modified external triggering mode.

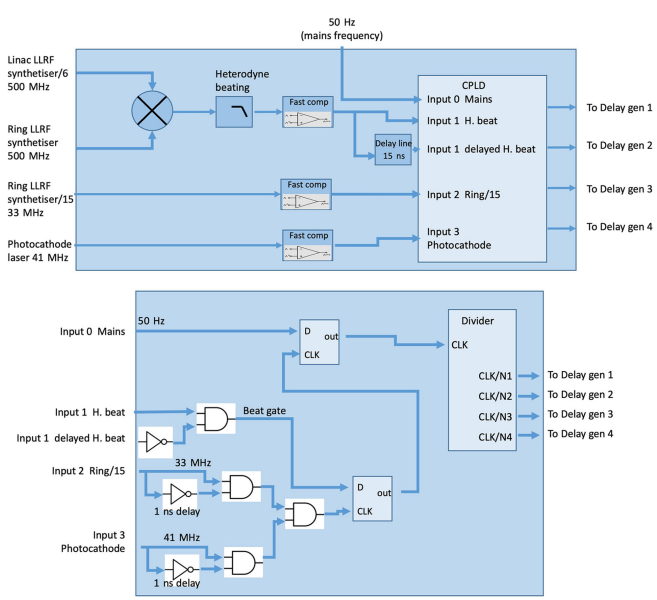

FIG. 37. Block diagram of the heterodyne trigger generation system (top) and zoom on the CPLD (bottom).

Four delay generators are used, one for the modulator, one for the Linac, one for the ring, and one for the diagnostics. Each one has between 10 and 20 outputs. As shown in Fig. 37, they can operate at different submultiples of the main frequency. To allow the prefiring of some equipment, the reference trigger was initially set to, but this proved to be not enough, so it was set to −50 μs before the time at which the laser pulse hits the photocathode. As the repetition rate is currently limited to 10 Hz by the French Nuclear Safety Authority, only the modulator's delay generator operates at 50 Hz, the other operates at 10 Hz or below.

E. Results

The measurements presented below were done with a Lecroy 760Zi oscilloscope. The jitter noise floor is around 1 ps (rms), meaning that a 1° (rms) phase jitter measurement is achievable with respect to the highest frequency of the input signals. In this section, we call "jitter" a variation measured in a 10 s time gate and "drift" a variation over a longer period of a quantity averaged during 20 s. The following jitter and drift measurements were carried out: (i) The jitter between the LLRF signal from the ring (500 MHz) and the LLRF signal from the output of the divider by 15 (33.3 MHz): it has been found to be below the oscilloscope resolution. A drift was measured at a value of around 1 ps/h (see Fig. 38). (ii) The jitter between the LLRF signal from the Linac divided by 6 (500 MHz) and the signal from the photocathode laser (41.64 MHz): measurement attempts have shown that it is below the oscilloscope resolution. The laser interface displays a jitter below 100 fs. (iii) The jitter between the LLRF signal from the Linac divided by 6 (500 MHz) and the LLRF signal from the ring 500 MHz at injection time (10 Hz): a jitter has been measured below 7 ps (rms) and below 30 ps (full width at 10% of the maximum), as shown in Fig. 39(a). Drift is negligible over the 2h30 period of data acquisition. (iv) The jitter between the LLRF signal from the ring

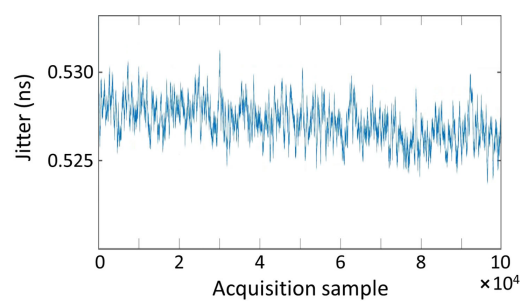

FIG. 38. Relative time between a fixed phase of the LLRF signal from the ring (500 MHz) and a fixed phase of the LLRF signal from the output of the divider by 15 (33.3 MHz). The acquisition frequency is 10 Hz. A small drift is observed with a slope of about 1 ps/h.

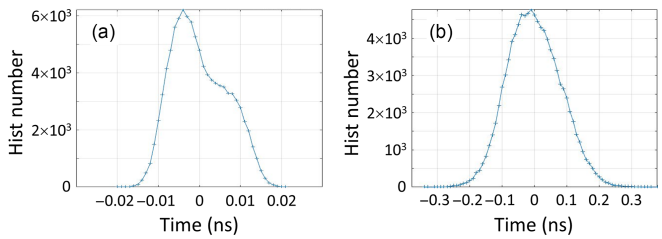

FIG. 39. (a) Relative time between a fixed phase of the LLRF signal from the Linac divided by 6 (500 MHz) and a fixed phase of the LLRF signal from the ring (500 MHz). (b) Relative time between a fixed phase of the LLRF signal from the ring (500 MHz) and the injection trigger (10 MHz).

500 MHz and the injection trigger (10 Hz): a jitter has been measured below 100 ps (rms) and below 360 ps (full width at 10% of the maximum), as shown in Fig. 39(b). Drift is lower than 400 ps over the 2h30 period of data acquisition.

To quickly identify and diagnose possible issues related to the noise in a system, an automated monitoring system has been installed based on a Wavecatcher digitizer [45] that monitors jitters between the signals.

If the trigger signal does not come within a certain time window after the previous one (20 ms $\pm$ 500 ps), the rf chain will not fire and thus there will be no electrons accelerated. This misfire due to trigger lateness has been studied in detail and can occur when the ratio between the Linac frequency and the ring frequency is a rational number. As shown in Fig. 40, moving the Linac frequency by a few hundred hertz (out of 2998.55 MHz) can solve the problem while being transparent for all the devices.

F. Current status and future upgrades

The synchronization system performances are good enough to generate x-rays by Compton interaction. However, the following issues have to be understood and addressed: (i) The jitter between the "real" laser pulse train in the Fabry-Perot cavity and the LLRF signal synthesizer is unknown. This has to be studied and minimized to maximize the x-ray flux. Longtime drifts have also to be understood and addressed. The same considerations are made for the "real" electron bunches in the ring. (ii) The drift of the Linac LLRF with respect to the 10 Hz trigger has not yet been measured. If it is too high, this could create difficulties with the firing time of the pulsed elements with runs lasting several hours. (iii) Drifts have been observed between the rf signal arrival at the gun and the laser arrival time. This can be due to thermal effects in the transport of these signals. A drift compensation scheme has been developed but not yet installed.

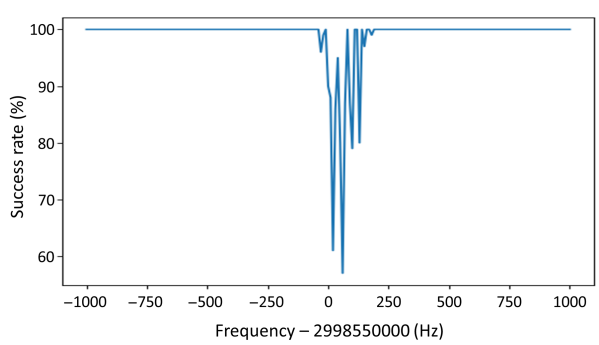

FIG. 40. Fraction of trigger misfires (vertical axis) as a function of Linac frequency (for a ring frequency of 500.250 MHz). Shifting the Linac frequency by a few hundred hertz is sufficient to prevent these misfires.

VII. X-RAY BEAMLINE AND RESULTS

A. X-line description

The x-ray beamline is divided into two distinct parts. The first is located inside the bunker (named "x-ray table" in Fig. 1), and the second inside a dedicated X-hutch. A photograph of the first part is shown in Fig. 41. It is located 1.8 m downstream of the Compton interaction point. It consists of a motorized optical table on which are positioned several devices, shown in Fig. 42, for both continuous beam control (intensity and position) and beam shaping. The table is manually retractable for access to the Fabry-Perot cavity. Starting from the beginning of the table (left to right), the different elements are as follows: (i) A beam shutter used for background measurement and subtraction [Fig. 42(a)]. (ii) A pair of double slits made of tungsten plates for selecting a part of the beam [Fig. 42(b)]. (iii) A fluorescent screen detector [Fig. 42(c)] made of a ZnCdS screen, retractable remotely and coupled with a photodiode and a camera used for the relative intensity measurement and beam spatial profile. The screen absorbs an important part of the beam. (iv) A homemade detector [Fig. 42(e)] consisting of a Kapton foil inserted into the beam, coupled to two photodiodes mounted on a linear stage for adjusting their distance to the foil according to the beam size selected by the slits [Fig. 42(b)]. X-rays scattered by the Kapton are detected by the photodiodes. The sum and difference of the photodiode currents are used to monitor variations in beam flux and position. This monitor

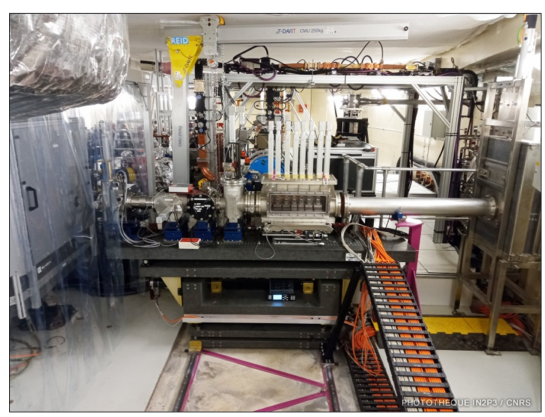

FIG. 41. Photograph of the X-line part located in the bunker.

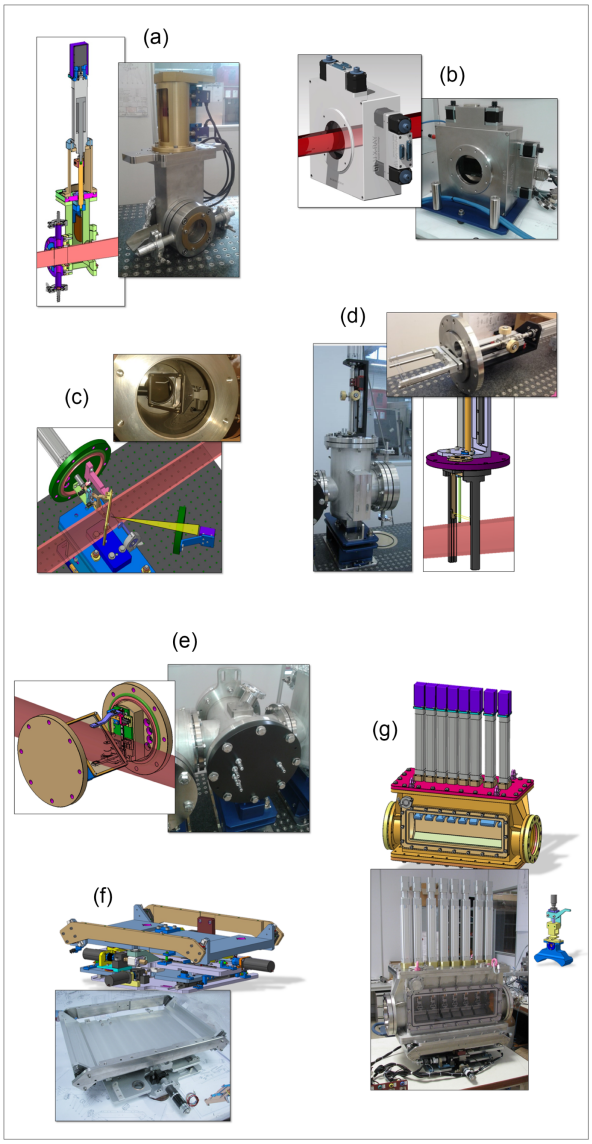

FIG. 42. Elements of the first part of the X-line. (a) Beam shutter. (b) Double slits. (c) Fluorescent screen detector. (d) Wire monitor. (e) Diffusion detector. (f) Transfocator alignment table. (g) Focusing device (transfocator).

can remain continuously in the beam since the absorption of the Kapton foil is completely negligible. (v) A wire monitor [Fig. 42(d)] consisting of two tungsten wires that can be moved along the beam to monitor the beam position. (vi) An optical device [Fig. 42(g)] called "a transfocator" [67] made of refractive aluminum lenses put in six racks mounted on an inserting system. It is used to focus or make parallel the beam on samples located at approximately 10 m from the interaction point. The two end racks are equipped with pinholes for beam centering. This transfocator is supported by a small motorized table [Fig. 42(f)] for precise beam alignment.

To carry out experiments for demonstrating the potential and the limits of the ThomX demonstrator, a second set of

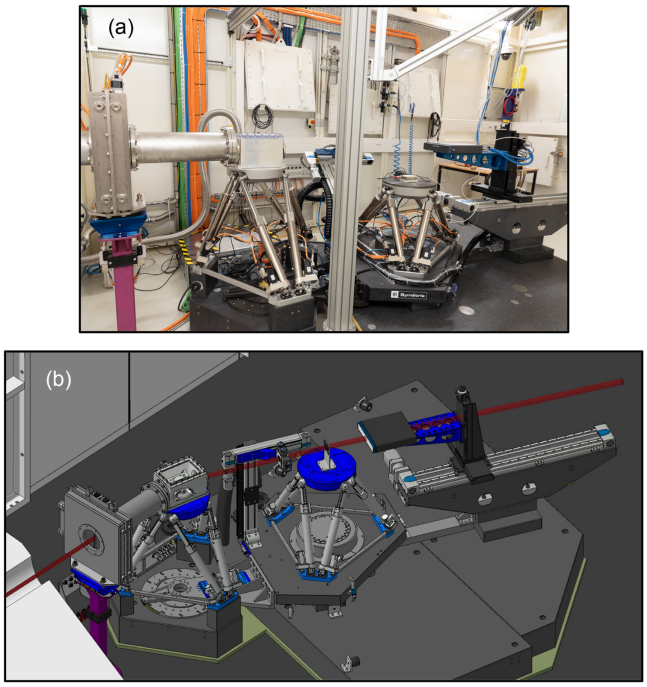

FIG. 43. Photograph of the experimental setup in the X-hutch (a) and schematic 3D mechanical view (b).

equipment is installed inside an experimental hutch after a safety beam shutter and the concrete wall of the accelerator bunker. X-rays are transported from the bunker to the experimental area through a vacuum beam pipe. This second part of the beamline is shown in Fig. 43 and consists of various elements that will be used depending on the analysis technique implemented.

At the entrance of the hutch, the maximum beam of 15 cm diameter (corresponding to the beam pipe diameter) is spatially selected and cleaned with a pair of double slits. A first hexapod is used to precisely align a monochromator based on Si(111) crystal. The monochromator can be completely retracted from the beam. Next, a second hexapod allows to position the sample, and a third series of slits is used to clean the beam just before the sample. A rotation stage, mounted on the sample hexapod, enables tomography. Both hexapodes (from Symétrie Company) have a micrometer precision level. Also, the sample hexapod can rotate around the monochromator one, enabling the desired beam energy to be selected according to a given monochromator position. At the end of the line, a detector arm can be fitted with a cross table for positioning a detector or an analyzer assembly Soller slits type. Both can be positioned also along the beam axis. Finally, the detector arm can be rotated around the sample (to select the different diffraction peaks, for example).

A set of detectors presented in Fig. 44 is also available to characterize the x-ray line and perform analyses: (i) For the absolute x-ray flux measurement, a 300 mm^2 silicon (Si) photodiode of 1 mm thickness, calibrated at Physikalisch-Technische Bundesanstalt in the 20–60 keV range; (ii) for

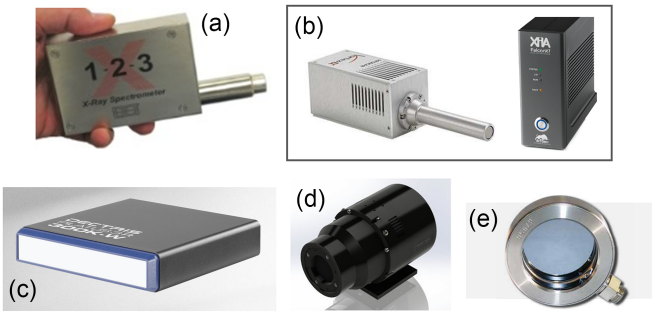

FIG. 44. Available detectors on the x-ray line of ThomX: (a) the CdTe spectrometer, (b) the Si spectrometer and its readout electronics, (c) the CdTe camera, (d) the sCMOS camera, and (e) the calibrated Si photodiode.

high-energy x-ray fluorescence measurements and x-ray beam characterization, a compact cadmium telluride (CdTe) crystal spectrometer of 1 mm thickness, 5×5 mm^2 of active area, with an integrated electronics; (iii) for low-energy x-ray fluorescence measurements, two identical Si crystal spectrometers of 1 mm thickness, 50 mm^2 of active area, with a high counting rate electronic readout ($\sim$1 Mcts/s); (iv) for high-resolution imaging, a sCMOS camera coupled to a CsI scintillator, with a resolution of a few tens of microns, an active input area of 55×55 mm^2, a slow readout of $\sim$10 frame/s; and (v) for x-ray diffraction patterns measurements or lower resolution imaging, a CdTe camera with an active area of 253×33 mm^2 and 172 μm pixel size.

B. First x-ray results on ThomX

In summer 2023, the first x-rays were detected [68]. X-ray production was done in a nonsynchronized mode between electron bunches and laser pulses from a locked Fabry-Perot cavity, and with the storage ring nominal optics working at 500.38 MHz (see Sec. III B). In this mode, where the electron bunches and laser pulses crossed each other randomly, the total flux measured with the fluorescent screen detector shown in Fig. 42(c) (located in the ThomX bunker at 2.4 m from the Compton IP) was estimated to $\sim 10^7$ x-ray/s [68]. This detector had previously been calibrated during a series of measurements on a beamline at the ESRF synchrotron. To derive this flux value, the correction of the detector angular acceptance was applied for a measured electron beam energy of 50 MeV ($\gamma = 97.8$). Then, the vertical electron beam size at the IP was measured by scanning vertically the Fabry-Perot optical table. The result gave an electron beam size of about 80 μm, in good agreement with the predicted value [68].

Recently, the synchronization has been set up and allowed around 10^{10} ph/s to be produced. X-ray production in this synchronization mode is illustrated in Fig. 45, which shows the signal recorded in the fluorescent screen detector as a function of time, taking into account detector calibration and detector angular acceptance.

The flux was also measured in the experimental area with the calibrated Si photodiode. The picoammeter current is shown as a function of time in Fig. 46 (left). Also presented are the histograms of the upper part of the signal (top right plot) corresponding to the times when the x-rays are produced and the lower part (bottom right plot) that is the measurement of the detector offset (no x-rays are produced). By taking into account the detector angular acceptance (300 mm^2 diode positioned at 10.5 m from the IP), this measurement using the calibrated photodiode leads to a total x-ray flux of $\sim 0.8 \times 10^{10}$ ph/s, in good agreement with the measurement performed in the bunker with the fluorescent screen detector. For this x-ray production, the laser power stored in the Fabry-Perot cavity was $\sim$90 kW (measured at cavity mirror transmission), the average electron charge stored in the ring of the order of 40 pC (estimated).

As illustrated in Fig. 45, x-ray production is not yet stable. The reason for this is mainly, on one hand numerous optical cavity power losses and, on the other hand, fluctuations of the stored electron beam. With the ThomX parameters given in Table I, simulations show that measured synchronization jitters (see Secs. V B and VI E) should lead to flux dispersion of less than 1%–2% and then cannot be responsible for the large fluctuations measured on the x-ray flux. In contrary, simulated electron beam vertical and horizontal position jitters of 50 μm and 150 μm, respectively, (i.e., typical values in the ThomX ring at present) should lead to flux dispersion of around 13% and 22%, respectively. Jitter of the stored charge, from one storage to the next, has been observed to be of the order of 10%–20% during our data acquisition (but has not yet been properly measured) and is directly transmitted to the flux. These simulation results are fairly consistent with the flux dispersion shown in Fig. 45 (i.e., around 30% peak-to-peak during periods when the optical cavity is locked). In the near future, we will work on the reduction of optical cavity

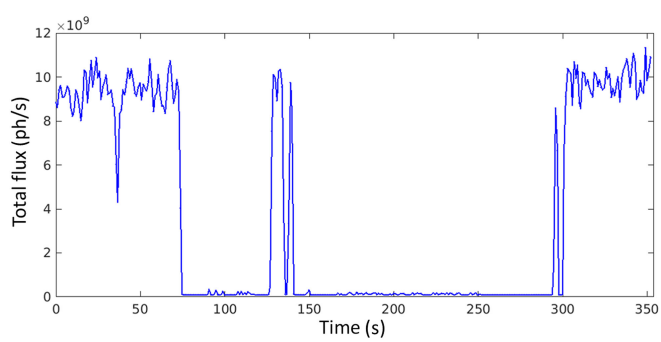

FIG. 45. Total flux of x-ray (ph/s) as a function of time, measured with the fluorescent detector in the bunker, after calibration and correction of the angular acceptance.

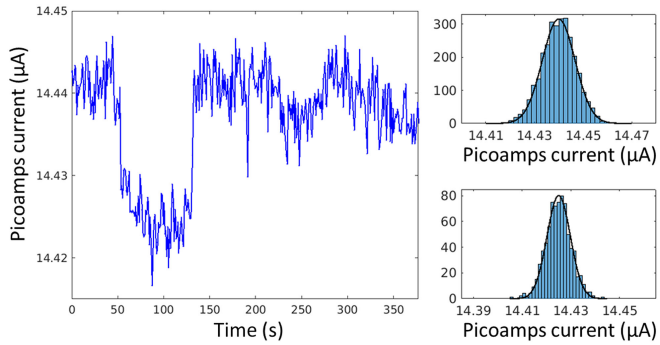

FIG. 46. Picoammeter signal from the calibrated photodiode as a function of time, measured in the X-hutch (left). Histogram of the high part of the signal (right up), and of the low part of the signal (right down).

unlocking times. In addition, studies of the electron beam in the ring will be carried out to evaluate experimentally the effect of spatial perturbations, orbit quality, and storage quality on x-ray flux stability. This will help guide the fine-tuning of the ring optics.

Figure 47 shows the on-axis x-ray spectrum, normalized to its maximum value, measured with the compact CdTe spectrometer [see Fig. 44(a)] positioned on the sample hexapod (see Fig. 43) at ∼10.6 m from the Compton IP. For this measurement, the x-ray beam was cleaned with the first pair of slits (located in the bunker) to suppress background noise due to multiple scattering that might occur along the beam path. Low-energy peaks due to photons escaping after interactions with Cd and Te inside the detector are visible in the figure (around 18 and 22 keV) and have been used to calibrate the detector thanks to the knowledge of the K_α and K_β emission lines of the Cd and Te. X-ray peak energy is 45.3 keV and the FWHM is 2.4 keV, demonstrating the quasimonochromaticity property of the Compton process.

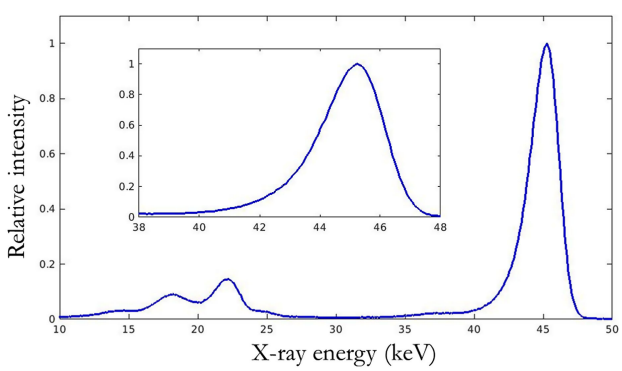

FIG. 47. ThomX on-axis x-ray spectrum acquired with the compact CdTe spectrometer [see Fig. 44(a)]. The small peaks around 18 and 22 keV are due to secondary x-rays produced by interaction with Cd or Te and escaping from the detector. The inset provides a close-up view of the Compton peak.

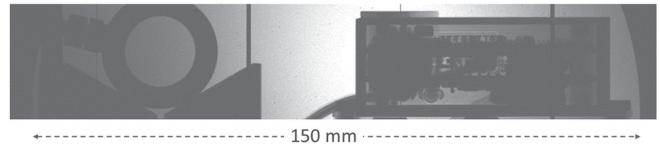

FIG. 48. First "radiography" recorded with the CdTe camera in the X-hutch showing the calibrated Si photodiode (at left) and the compact CdTe spectrometer (at right).

The first "radiography" taken in the experimental area is shown in Fig. 48. The image was acquired with the CdTe pixel camera. The calibrated photodiode (left in the image) and the compact CdTe spectrometer (right), both positioned on the sample hexapod, are visible.

These first ThomX results can be compared with the performances of other Compton source projects based on a laser enhancement cavity (sources that have been or are currently in operation), namely: (i) the KEK project [69] at the superconducting rf test facility that produced in 2015 10^7 ph/s at an energy of 29 keV; (ii) the LUCX source [70] that used a burst-mode laser pulse storage technique at the KEK-LUCX compact linear accelerator and produced in 2015 10 keV x-rays with a flux of 10^7 ph/s; (iii) the ERL-based LCS source project [71] that used the KEK compact energy recovery linac (cERL) and produced in 2016 7 keV x-rays with a flux of 10^7 ph/s; and (iv) the MuCLS source [72], based on a small electron storage ring, that currently produces 15– 35 keV x-rays with a flux of 10^{11} ph/s. The flux values given above correspond to x-ray production over the full bandwidth.

VIII. CONCLUSIONS AND PERSPECTIVES

We have reported the first steps of the commissioning of the ThomX x-ray source. First electron bunches were produced at the photoinjector, focused at the entrance to the accelerating section, and transmitted to the end of the Linac. The charge and energy measured were 100 pC and 50 MeV, respectively, i.e., maximum values that were authorized by the French ASN at that time. Then, the beam was sent into the transfer line, injected, and stored in the ring. Storage was successfully achieved. Regarding the commissioning of the interaction laser system, the laser was locked successfully in the Fabry-Perot cavity despite the noisy environment created by the accelerator. The first x-rays were produced with a flux around 10^7 ph/s in nonsynchronized electron/laser mode. Then, ThomX moved to the production of $\sim 10^{10}$ x-rays/s after the commissioning of the synchronization system. During this phase, finding that the ring's natural frequency was significantly above the design value from 300 to 400 kHz, we have developed a solution based on a temporary ring optic. This issue will be resolved in the near future by increasing the circumference of the ring by ∼14 mm.

TABLE II. Current and future electron, laser, and x-ray beam parameters.

Parameter	Today	Near future	Distant future	Unit
Injection frequency	10	50	50	Hz
e- energy	50	50–70	50–70	MeV
Average stored e- charge	40	200	1000	pC
Average stored laser power	90	500	700	kW
e- spot size at IP (rms)	77	77	77	μm
Laser spot size at IP (rms)	65	40	40	μm
X-ray Compton edge	45	45–90	45–90	keV
Average total flux	1.0×10^{10} not stable	1.5×10^{12} stable	1.0×10^{13} stable	ph/s

The next step toward nominal parameters will be to increase the energy and charge of the electron bunches, increase the average power stored in the optical cavity [63,64], reduce the size of the laser beam spot at the interaction point, reduce the synchronization jitters, and shorten the unlocking periods of the Fabry-Perot cavity. All this should lead to a stable flux of 10^{12} ph/s in the energy range of 45–90 keV. In the more distant future, we will strive to store in the ring and in the optical cavity the nominal electron bunch charge and laser power (1 nC and 700 kW, respectively). These milestones are summarized in Table II.

In parallel, the characterization of the x-ray beam and source brightness will be measured with the available X-line equipment, and the main analysis techniques used in x-ray research will be qualified. In standard imaging, propagation-based phase contrast imaging, K-edge subtraction imaging, and tomography, we will measure spatial resolution, contrast, and sensitivity to contrast drugs thanks to phantoms of low-density materials with properties comparable to those of soft tissue. Also, after the commissioning of the monochromator and the focusing device, we will qualify our different systems "source + detector" in terms of sensitivity and resolution in fluorescence spectroscopy and diffraction analysis techniques. Concurrently, detailed electron beam physics studies will be conducted in the storage ring to finalize the commissioning phase. These studies will encompass optics investigations, LOCO (Linear Optics from Closed Orbits) analysis [73], tuning of feedback systems, and other relevant aspects to ensure the delivery of nominal performances. Furthermore, as beam intensity rises, investigations into the impact of collective effects on longitudinal electron beam dynamics will be pursued, particularly pertinent for compact Compton sources.

ThomX represents a new compact Compton scattering x-ray source, incorporating state-of-the-art components developed through extensive R&D efforts focused on the Fabry-Perot cavity, synchronization, ring, and overall compactness. The commissioning presented significant challenges, requiring a lot of effort and expertise.

ACKNOWLEDGMENTS

The present work was financed by the French National Research Agency (ANR) under the Equipex program ANR-EQPX-51.

[1] P. Walter *et al.*, A new high quality X-ray source for Cultural Heritage, C. R. Phys. **10**, 676 (2009).

[2] M. Jacquet *et al.*, Potential of compact Compton sources in the medical field, Phys. Med. **32**, 1790 (2016).

[3] B. Günther *et al.*, The versatile X-ray beamline of the Munich Compact light ource: Design, instrumentation and applications, J. Synchrotron Radiat. **27**, 1395 (2020).

[4] L. Federici *et al.*, Backward Compton scattering of laser light against high-energy electrons: The LADON photon beam at Frascati, Il Nuovo Cimento B (1971–1996) **59**, 247 (1980).

[5] Z. Huang and R. D. Ruth, Laser-electron storage ring, Phys. Rev. Lett. **80**, 976 (1998).

[6] S. Baudrand *et al.*, A high precision Fabry-Perot cavity polarimeter at HERA, J. Instrum. **5**, P06005 (2010).

[7] J. Bonis *et al.*, Non-planar four-mirror optical cavity for high intensity gamma ray flux production by pulsed laser beam Compton scattering off GeV-electrons, J. Instrum. **7**, P01017 (2012).

[8] A. Börzsönyi *et al.*, External cavity enhancement of picosecond pulses with 28,000 cavity finesse, Appl. Opt. **52**, 8376 (2013).

[9] I. Chaikovska *et al.*, High flux circularly polarized gamma beam factory: Coupling a Fabry-Perot optical cavity with an electron storage ring, Sci. Rep. **6**, 36569 (2016).

[10] T. Suzuki, General formulas of luminosity for various types of colliding beam machines, National Laboratory for High Energy Physics, Oho, Ibaraki, Report No. KEK-76-3, 1976.

[11] A. Variola *et al.*, ThomX technical design report, LAL, Report No. LAL/RT 14-21, 2014.

[12] K. Dupraz *et al.*, The ThomX ICS source, Phys. Open **5**, 100051 (2020).

[13] J. Brossard *et al.*, Construction of the probe beam photo-injector of CTF3, in *Proceedings of the 10th European Particle Accelerator Conference, EPAC-2006, Edinburgh,*

Scotland (JACoW, Geneva, Switzerland, 2006), pp. 828–830.

[14] B. E. Carlsten, New photoelectric injector design for the Los Alamos National Laboratory XUV FEL accelerator, Nucl. Instrum. Methods Phys. Res., Sect. A **285**, 313 (1989).

[15] L. Serafini and J. B. Rosenzweig, Envelope analysis of intense relativistic quasilaminar beams in rf photoinjectors: A theory of emittance compensation, Phys. Rev. E **55**, 7565 (1997).

[16] R. Belbeoch *et al.*, Rapport d'etudes sur le projet des linacs injecteur de LEP (LIL), LAL, Report No. LAL/PI/82-01/T, 1982.

[17] B. Pottin *et al.*, HELIOS, the Linac injector of SOLEIL: Installation and first results, in *Proceedings of the Particle Accelerator Conference, PAC-2005, Knoxville, TN* (JACoW, Geneva, Switzerland, 2005), pp. 755–757.

[18] J. Orloff, *Handbook of Charged Particle Optics* (CRC Press, Boca Raton, FL, 2008).

[19] T. Vinatier *et al.*, Analytical modeling of longitudinal beam dynamics in an RF-gun: rom almost zero to relativistic velocities, Nucl. Instrum. Methods Phys. Res., Sect. A **953**, 162914 (2020).

[20] H. Purwar *et al.*, Random error propagation on electron beam dynamics for a 50 MeV S-band linac, J. Phys. Commun. **7**, 025002 (2023).

[21] K. Flöttmann, ASTRA, A Space Charge Tracking Algorithm, 2017, https://www.desy.de/~mpyflo/Astra_manual/Astra-Manual_V3.2.pdf.

[22] M. Alkadi *et al.*, Electromagnetic and beam dynamics studies of the ThomX Linac, in *Proceedings of the 12th International Particle Accelerator Conference, IPAC-2021, Campinas, Brazil* (JACoW, Geneva, Switzerland, 2021), pp. 2721–2724.

[23] M. C. Ross *et al.*, Automated emittance measurements in the SLC, Conf. Proc. C **870316**, 725 (1987).

[24] I. M. Kapchinskij and V. V. Vladimirskij, Limitations of proton beam current in a strong focusing linear accelerator associated with the beam space charge, in *Proceedings of the 2nd International Conference on High-Energy Accelerators, HEACC-1959, Geneva, Switzerland* (CERN, Geneva, Switzerland, 1959), pp. 274–288, https://inspirehep.net/literature/919865.

[25] G. Franchetti, Space charge in circular machines, in *Proceedings of the CAS-CERN on Intensity Limitations in Particles Beams, Geneva, Switzerland* (CERN, Geneva, Switzerland, 2015).

[26] M. Borland, A high-brightness thermionic microwave electron gun, Ph.D. thesis, SLAC National Accelerator Laboratory, 1991.

[27] H. Grote and F. C. Iselin, The MAD program (methodical accelerator design), CERN Report No. CERN/SL/90-13, 1994, https://inspirehep.net/literature/214504.

[28] A. Moutardier, Study and optimization of a compact X-ray source, Ph.D. thesis, Université Paris-Saclay, 2022.

[29] A. Variola *et al.*, ThomX conceptual design report, IN2P3, Report No. LAL RT 09/28-SOLEIL/SOU-RA-2678, 2010, https://in2p3.hal.science/in2p3-00448278.

[30] I. Drebot, Electron beam dynamics with and without Compton back scattering Ph.D. thesis, Université Paris-Sud, 2013.

[31] A. Gamelin *et al.*, Longitudinal and transverse dynamics of ions from residual gas in an electron accelerator, Phys. Rev. Accel. Beams **21**, 054401 (2018).

[32] A. Gamelin, Collective effects in a transient microbunching regime and ion cloud mitigation in ThomX, Ph.D. thesis, Université Paris-Saclay, 2018.

[33] A. Gamelin *et al.*, Longitudinal impedance and coherent synchrotron radiation models for ThomX storage ring, Nucl. Instrum. Methods Phys. Res., Sect. A **999**, 165191 (2021).

[34] V. Kubytskyi *et al.*, Commissioning of the ThomX storage ring, in *Proceedings of the 14th International Particle Accelerator Conference, IPAC-2023, Venice, Italy* (IOP Publishing, Bristol, UK, 2024), Vol. 2687, p. 032031.

[35] X. Huang *et al.*, An algorithm for online optimization of accelerators, Nucl. Instrum. Methods Phys. Res., Sect. A **726**, 77 (2013).

[36] H. Wiedemann, *Particle Accelerator Physics* (Springer Nature, Switzerland, 2015), 10.1007/978-3-319-18317-6.

[37] M. Akemoto *et al.*, Construction and commissioning of the compact energy-recovery linac at KEK, Nucl. Instrum. Methods Phys. Res., Sect. A **877**, 197 (2018).

[38] M. Arnold *et al.*, First ERL operation of S-DALINAC and commissioning of a path length adjustment system, in *Proceedings of the 9th International Particle Accelerator Conference, IPAC-2018, Vancouver, BC Canada* (JACoW, Geneva, Switzerland, 2018), pp. 4859–4862.

[39] Dassault Systèmes, Opera, 2022, https://www.3ds.com/products-services/simulia/products/opera/.

[40] A. Terebilo, Accelerator toolbox for MATLAB, SLAC, Report No. SLAC-PUB-8732, 2001, https://inspirehep.net/literature/557783.

[41] A. Latina, *RF-Track Reference Manual* (2021), 10.5281/zenodo.4580369.

[42] A. Moutardier *et al.*, Characterization of the electron beam visualization stations of the ThomX accelerator, J. Phys. Conf. Ser. **2420**, 012065 (2023).

[43] S. D. Williams *et al.*, Lens calibration for beam size monitors at ThomX, in *Proceedings of the 9th International Beam Instrumentation Conference, IBIC-2020, Santos, Brazil* (JACoW, Geneva, Switzerland, 2020), pp. 281–284.

[44] N. Delerue *et al.*, Tests of a 3D printed BPM with a stretched wire and with a particle beam, in *Proceedings of the 10th International Particle Accelerator Conference, IPAC-2019, Melbourne, Australia* (JACoW, Geneva, Switzerland, 2019), pp. 4368–4371.

[45] D. Breton *et al.*, The WaveCatcher family of SCA-based 12-bit 3.2-GS/s fast digitizers, in *Proceedings of the 19th Real-Time Conference, RT2014* (2014), https://in2p3.hal.science/in2p3-00995691.

[46] I. Chaikovska *et al.*, Real-time display system for the optical fiber beam loss monitor for the PHIL and ThomX facilities, in *Proceedings of the third International Beam Instrumentation Conference, IBIC-2014, Monterey, CA* (JACoW, Geneva, Switzerland, 2014), pp. 463–467.

[47] H. Kogelnik and T. Li, Laser beams and resonators, Appl. Opt. **5**, 1550 (1966).

[48] L. Amoudry, Etude de cavités Fabry-Perot de hautes finesses pour le stockage de fortes puissances moyennes.

Application à la source compacte de rayons X ThomX, Ph.D. thesis, Université Paris-Saclay, 2021.

[49] M. Amer, Optical R&D to reach ThomX ultimate performance, Ph.D. thesis, Université Paris-Saclay, 2023.

[50] A. Martens *et al.*, Design of the optical system for the gamma factory proof of principle experiment at the CERN Super Proton Synchrotron, Phys. Rev. Accel. Beams **25**, 101601 (2022).

[51] P. Favier, Etude et conception d'une cavité Fabry-Perot de haute finesse pour la source compacte de rayons X ThomX, Ph.D. thesis, Université Paris-Saclay, 2017.

[52] F. Labaye, Amplification passive d'un laser à fibre optique dans une cavité Fabry-Perot: Application à la production de rayonnement gamma par diffusion Compton inverse, Ph.D. thesis, Université Paris-Sud, 2012.

[53] F. Zomer *et al.*, Polarization induced instabilities in external four-mirror Fabry-Perot cavities, Appl. Opt. **48**, 6651 (2009).

[54] J. A. Arnaud, Nonorthogonal optical waveguides and resonators, Bell Syst. Tech. J. **49**, 2311 (1970).

[55] H. Wang *et al.*, Prior-damage dynamics in a high-finesse optical enhancement cavity, Appl. Opt. **59**, 10995 (2020).

[56] A. F. Brooks *et al.*, Point absorbers in advanced LIGO, Appl. Opt. **60**, 4047 (2021).

[57] H. Carstens *et al.*, Megawatt-scale average-power ultrashort pulses in an enhancement cavity, Opt. Lett. **39**, 2595 (2014).

[58] C. Locke *et al.*, A simple technique for accurate and complete characterisation of a Fabry-Perot cavity, Opt. Express **17**, 21935 (2009).

[59] P. Hello and J.-Y. Vinet, Analytical models of thermal aberrations in massive mirrors heated by high power laser beams, J. Phys. **51**, 1267 (1990).

[60] A. L. Bullington *et al.*, Modal frequency degeneracy in thermally loaded optical resonators, Appl. Opt. **47**, 2840 (2008).

[61] L. Amoudry *et al.*, Modal instability suppression in a high-average-power and high-finesse Fabry–Perot cavity, Appl. Opt. **59**, 116 (2020).

[62] R. W. Drever *et al.*, Laser phase and frequency stabilization using an optical resonator, Appl. Phys. B **31**, 97 (1983).

[63] X.-Y. Lu *et al.*, Stable 500 kW average power of infrared light in a finesse 35,000 enhancement cavity, Appl. Phys. Lett. **124**, 251105 (2024).

[64] X.-Y. Lu *et al.*, 710 kW stable average power in a 45,000 finesse two-mirror optical cavity, Opt. Lett. **49**, 6884 (2024).

[65] N. Delerue *et al.*, Synchronization of a photo-injector and a high power laser with independent clocks, in *Proceedings of the 8th International Particle Accelerator Conference, IPAC-2017, Copenhagen, Denmark* (JACoW, Geneva, Switzerland, 2017), pp. 3935–3937.

[66] N. Delerue *et al.*, The synchronization system of the Thomx accelerator, in *Proceedings of the 9th International Particle Accelerator Conference, IPAC-2018, Vancouver, BC Canada* (JACoW, Geneva, Switzerland, 2018), pp. 2243–2246.

[67] A. Snigirev *et al.*, A compound refractive lens for focusing high-energy x-rays, Nature (London) **384**, 49 (1996).).

[68] M. Jacquet *et al.*, First production of X-rays at the ThomX high-intensity Compton source, Eur. Phys. J. Plus **139**, 459 (2024).

[69] H. Shimizu *et al.*, X-ray generation by inverse Compton scattering at the superconducting RF test facility, Nucl. Instrum. Methods Phys. Res., Sect. A **772**, 26 (2015).

[70] K. Sakaue *et al.*, Laser-Compton scattering X-ray source based on normal conducting Linac and optical enhancement cavity, in *Proceedings of the 6th International Particle Accelerator Conference, IPAC-2015, Newport News, VA* (JACoW, Geneva, Switzerland, 2015), pp. 1635–1637.

[71] T. Akagi *et al.*, Narrow-band photon beam via laser Compton scattering in an energy recovery linac, Phys. Rev. Accel. Beams **19**, 114701 (2016).

[72] E. Eggl *et al.*, The Munich compact light source: Initial performance measures, J. Synchrotron Radiat. **23**, 1137 (2016).

[73] I. Chaikovska *et al.*, Lattice correction using LOCO for the ThomX storage ring, in *Proceedings of the 6th International Particle Accelerator Conference, IPAC-2015, Newport News, VA* (JACoW, Geneva, Switzerland, 2015), pp. 117–120.